Geophysical Journal International

*Geophys. J. Int.* (2025) **242,** 1–24
Advance Access publication 2025 July 16
Research Paper

https://doi.org/10.1093/gji/ggaf271

# Ocean-bottom seismic interferometry in coupled acoustic–elastic media

Adesh Pandey [1], Sjoerd de Ridder [2], Jeffrey Shragge [1] and Aaron J. Girard [1]

[1] *Center for Wave Phenomena, Department of Geophysics, Colorado School of Mines, Golden CO* 80401, *USA. E-mail: adesh0805@gmail.com*
[2] *School of Earth and Environment, University of Leeds, Leeds LS2 9JT, UK. E-mail: S.Deridder@leeds.ac.uk*

Accepted 2025 July 10. Received 2025 July 8; in original form 2025 March 25

## SUMMARY

Green's function expressions for seismic interferometry in acoustic and elastic media have been extensively studied and applied across a wide range of applications, including surface-wave tomography and generating virtual shot gathers. However, analogous expressions for coupled acoustic–elastic media systems remain absent, despite their importance for analysing cross-correlation wavefields from ocean-bottom nodal and seismometer recordings and other seismic problems in marine settings. To address this issue, we derive convolution- and correlation-type reciprocity relations for physically coupled acoustic–elastic media by combining Rayleigh's and Rayleigh–Betti reciprocity theorems, incorporating the constitutive equations governing coupling at the acoustic–elastic interface, and applying time-reversal invariance principles for an arbitrary 3-D inhomogeneous, lossless medium. The derived relationships show that the acoustic and elastic Green's functions between any two observation points in the medium can be expressed as integrals of cross-correlations of wavefield observations at those locations, generated by sources distributed over an arbitrarily shaped closed surface enclosing the two observation points. When the Earth's free surface coincides with the enclosing surface, integral evaluation is required only over the remaining portion of the closed surface. If the sources are mutually uncorrelated ambient sources, the Green's function representation simplifies to a direct cross-correlation of wavefield observations at the two points, generated by a specific ambient source distribution on the closed surface. However, in practical scenarios, the ideal source distribution necessary to retrieve Green's functions is rarely realized, for example, due to non-uniform illumination. To address these challenges, we represent the ambient cross-correlations as self-consistent observations and introduce a cross-correlation modelling methodology that accounts for practical limitations in source distribution for coupled acoustic–elastic media scenarios. We illustrate the theory by modelling ambient cross-correlation wavefields for a deep-water scenario.

**Key words:** Empirical Green's function; Seismic interferometry; Surface waves and free oscillations; Theoretical seismology; Wave propagation.

## 1 INTRODUCTION

Recent advances in sparse, large-scale, multicomponent ocean-bottom sensor array deployments— including ocean-bottom seismometers (OBSs), cables (OBCs) and nodes (OBNs)—offer a unique opportunity to enhance our understanding of marine ambient wavefield phenomena by extracting low-frequency (sub-2.0 Hz) wavefield information at the seabed. Many continuous ocean-bottom acquisitions lasting for durations spanning one to three months are designed for active-source seismic exploration, where short-duration windows are extracted to form shot gathers, with the remainder of the data archived and often disregarded as containing little useful information for subsurface investigation—especially below the 2.0 Hz low-frequency cutoff of typical marine air-gun sources.

Long-time continuous seafloor recordings, though, also capture a rich broad-band spectrum of ambient seismic energy in the 0.01–1.0 Hz frequency range, and a growing number of studies demonstrate that this low-frequency energy can be transformed into useful surface-wave information through seismic interferometry (de Ridder & Dellinger 2011; Girard *et al.* 2023, 2024). For example, ambient virtual shot gather (VSG) volumes derived from continuous wavefield data recorded on OBC arrays at the Valhall (de Ridder & Dellinger 2011) and Ekofisk

(de Ridder & Biondi 2015) fields in the Norwegian North Sea, as well as OBN arrays in the Gulf of Mexico (Stewart 2006; Girard *et al.* 2023, 2024), reveal dispersive surface- and guided *P*-wave modes. These VSGs also exhibit surface-wave sensitivity to strong lateral velocity heterogeneities (e.g. salt bodies) within the sub-2.0 Hz frequency band. de Ridder & Dellinger (2011) further used VSG data for ambient eikonal tomography to perform near-seabed imaging at the North Sea Valhall field, while de Ridder & Biondi (2015) used VSG-derived dispersion panels to image Scholte-wave group velocities via straight-ray tomography. These examples demonstrate the potential of using the low-frequency information recorded on ocean-bottom sensors for subsurface investigation, complementing conventional exploration methods.

To fully exploit the potential of ambient VSG data and move towards low-frequency elastic Earth model building through full-waveform inversion (FWI), it is essential to understand the physical significance of the cross-correlated wavefield recorded on ocean-bottom sensors. This understanding requires interpreting ambient wavefield information within the context of marine settings characterized by physically coupled acoustic–elastic media and accurately modelling these wavefields for FWI workflows within an appropriate seismic interferometry (SI) framework. Consequently, it is imperative to develop Green's function representations for SI in such coupled-media systems, to understand when the underlying assumptions are realized, and to develop methodologies for using approximate representations for SI when they are not.

In SI, waves recorded at two receiver locations are correlated to approximate Green's function between these locations. Seismic wavefield energy, continuously generated by a diverse array of sources—including active sources, oceanic phenomena, and localized seismic events such as earthquakes—form the basis for such correlation-based interferometric analyses. Wapenaar & Fokkema (2006) provides a comprehensive overview of Green's function representations in terms of cross-correlations of full wavefields in arbitrary configurations (Weaver & Lobkis 2004; van Manen *et al.* 2006) and discusses modifications for their application in SI for both acoustic and elastodynamic systems, without assuming wavefield diffusivity. Lobkis & Weaver (2001), Wapenaar (2004) and Wapenaar & Fokkema (2006) demonstrate that the interstation correlation of ambient wavefields can approximate the interstation Green's function under the assumption of a diffused, equipartitioned, random and uncorrelated 'noise' field. Applications of Green's function retrieval using SI in acoustic and elastic systems have been extensively studied and successfully applied across various fields, including helioseismology (Rickett & Claerbout 2000), ultrasonics (Lobkis & Weaver 2001) as well as exploration (Bakulin & Calvert 2004) and global (Sager *et al.* 2018) seismology. However, Green's function representations for SI in coupled acoustic–elastic media, such as those encountered in ocean-bottom acquisition in marine environments, remain poorly studied and are notably absent from the literature.

This paper derives reciprocity relations for coupled acoustic–elastic systems by employing constitutive equations at the acoustic–elastic interface and reciprocity theorems for the associated acoustic and elastodynamic media. We establish source–receiver reciprocity expressions and give an overview of Green's function representations for pressure and particle velocity data in such systems, expressed through cross-correlations of full wavefields in arbitrary configurations within inhomogeneous, lossless media. We consider both open and free-surface configurations with approximations introduced to address practical SI challenges, including source availability and characteristics. For practical applications, we present a cross-correlation modelling (CCM) approach derived from Tromp *et al.* (2010) for realistically representing and modelling of ambient wavefield cross-correlations, supported by a synthetic simulation that highlights CCM waveform differences from the corresponding direct Green's function response.

## 2 RECIPROCITY FOR COUPLED ACOUSTIC–ELASTIC SYSTEMS

In many applications, such as exploration focused OBS deployments or globally focused marine seismic acquisition, waves propagating in an acoustic medium are physically coupled to wave motion in the underlying elastic solid through constitutive equations (Sun *et al.* 2017; Sethi *et al.* 2021). Fig. 1 illustrates the configuration of such a coupled domain where the acoustic medium, denoted as $V^{\mathrm{a}}$, is governed by acoustic wave-equation physics while wave propagation in the underlying elastic medium, denoted as $V^{\mathrm{e}}$, is described by the elastic wave equations.

### 2.1 Acoustic region

In the acoustic region $V^{\mathrm{a}}$, Rayleigh's reciprocity theorem (Rayleigh 1878; de Hoop 1988; Fokkema & van den Berg 1993; Wapenaar & Fokkema 2006) is given by:

$$\int_{V^{\mathrm{a}}} \left(\widehat{p}_{\mathrm{A}}\,\widehat{q}_{\mathrm{B}} - \widehat{v}_{\mathrm{i,A}}\,\widehat{f}_{\mathrm{i,B}} - \widehat{q}_{\mathrm{A}}\,\widehat{p}_{\mathrm{B}} + \widehat{f}_{\mathrm{i,A}}\,\widehat{v}_{\mathrm{i,B}}\right) \mathrm{d}^3\mathbf{x} = \oint_{\partial V^{\mathrm{a}}} \left(\widehat{p}_{\mathrm{A}}\,\widehat{v}_{\mathrm{i,B}} - \widehat{v}_{\mathrm{i,A}}\,\widehat{p}_{\mathrm{B}}\right) n_i^{\mathrm{a}}\,\mathrm{d}^2\mathbf{x} + \oint_{\partial V^{\cap}} \left(\widehat{p}_{\mathrm{A}}\,\widehat{v}_{\mathrm{i,B}} - \widehat{v}_{\mathrm{i,A}}\,\widehat{p}_{\mathrm{B}}\right) n_i^{\mathrm{a}}\,\mathrm{d}^2\mathbf{x}, \tag{1}$$

where $\widehat{p}(\mathbf{x}, \omega)$ and $\widehat{v}_i(\mathbf{x}, \omega)$ respectively represent the acoustic pressure and particle velocity with the A and B denoting two independent acoustic states; and $\widehat{f}_i(\mathbf{x}, \omega)$ and $\widehat{q}(\mathbf{x}, \omega)$ represent the source distributions in terms of external volume force density and volume injection rate density. Domain $V^{\mathrm{a}}$ represents an arbitrary acoustic spatial region enclosed by boundaries $\partial V^{\mathrm{a}}$ and $\partial V^{\cap}$ with the outward-pointing normal vector $\mathbf{n}^{\mathrm{a}} = n_i^{\mathrm{a}} = [n_1^{\mathrm{a}}, n_2^{\mathrm{a}}, n_3^{\mathrm{a}}]$, where the superscript $^{\mathrm{a}}$ indicates a quantity defined in the acoustic medium. The boundary $\partial V^{\cap}$ represents a coupled interface between the acoustic and elastic media (see Fig. 1). Lowercase Latin subscripts take values of 1, 2, 3, and $\mathbf{x} = [x_1, x_2, x_3]$ denotes the Cartesian coordinate vector with the $x_3$-axis oriented positive downwards. Finally, note throughout that the summation convention applies for repeated subscripts, and a circumflex accent over a variable [e.g. $\widehat{p}(\mathbf{x}, \omega)$] indicates a Fourier transformed quantity in the frequency

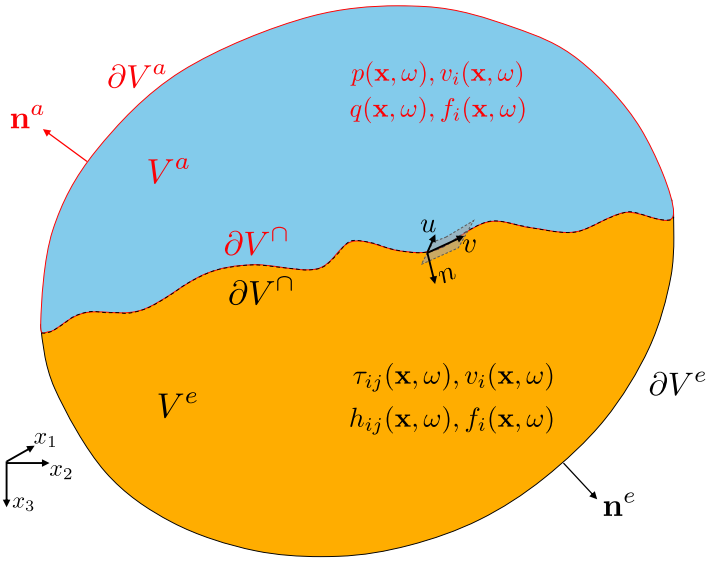


**Figure 1.** Configuration for a coupled acoustic ($V^{\mathrm{a}}$)-elastic ($V^{\mathrm{e}}$) system. The domains are coupled at common interface $\partial V^{\cap}$ by the constitutive equations. The sources acting in $V^{\mathrm{a}}$ include the volume injection rate density $q$, and volume force density $f_{\mathrm{i}}$, while the observed wavefields are the pressure $p$ and the particle velocity vector $v_{\mathrm{i}}$. In $V^{\mathrm{e}}$, the sources are the external deformation rate density $h_{ij}$ and the external volume force density $f_{\mathrm{i}}$, with the observed wavefields being the stress tensor $\tau_{ij}$ and the particle velocity vector $v_i$. The $uv$-plane shown is locally tangential to $\partial V^{\cap}$, with $n$ as the normal vector.

domain:

$$\widehat{p}(\mathbf{x},\omega) = \int_{-\infty}^{\infty} p(\mathbf{x},t)\,\exp(-\jmath\omega t)\,\mathrm{d}t, \tag{2}$$

where $\jmath$ is the imaginary unit and $\omega$ is angular frequency.

Eq. (1) represents the acoustic reciprocity theorem of the convolution type, where frequency-domain products (e.g. $\widehat{p}_{\mathrm{A}}\,\widehat{v}_{\mathrm{i,B}}$) correspond to convolutions in the time domain. The field and source quantities in eq. (1)—$\widehat{p}(\mathbf{x},\omega)$, $\widehat{v}_i(\mathbf{x},\omega)$, $\widehat{q}(\mathbf{x},\omega)$, and $\widehat{f}_i(\mathbf{x},\omega)$—satisfy the space-frequency-domain acoustic wave equations representing a coupled first-order system in a lossless, arbitrarily inhomogeneous fluid medium:

$$\jmath\omega\rho^{\mathrm{a}}\widehat{v}_i + \partial_i\widehat{p} = \widehat{f}_i \tag{3}$$

and

$$\jmath\omega\kappa^{\mathrm{a}}\widehat{p} + \partial_i\widehat{v}_i = \widehat{q}, \tag{4}$$

where $\partial_i$ denotes the partial derivative with respect to the $x_i$-direction; and $\rho^{\mathrm{a}} = \rho^{\mathrm{a}}(\mathbf{x})$ and $\kappa^{\mathrm{a}} = \kappa^{\mathrm{a}}(\mathbf{x})$ are the density and compressibility of the acoustic medium, respectively.

### 2.2 Elastic region

In elastic region $V^{\mathrm{e}}$, we express the Rayleigh-Betti reciprocity theorem (Knopoff & Gangi 1959; De Hoop 1966; Aki & Richards 2002; Wapenaar & Fokkema 2006) as

$$\begin{aligned}&\int_{V^{\mathrm{e}}} \left(-\widehat{\tau}_{ij,\mathrm{A}}\,\widehat{h}_{ij,\mathrm{B}} - \widehat{v}_{i,\mathrm{A}}\,\widehat{f}_{i,\mathrm{B}} + \widehat{h}_{ij,\mathrm{A}}\,\widehat{\tau}_{ij,\mathrm{B}} + \widehat{f}_{i,\mathrm{A}}\,\widehat{v}_{i,\mathrm{B}}\right)\,\mathrm{d}^3\mathbf{x}\\ &= \oint_{\partial V^{\mathrm{e}}} \left(\widehat{v}_{i,\mathrm{A}}\,\widehat{\tau}_{ij,\mathrm{B}} - \widehat{\tau}_{ij,\mathrm{A}}\,\widehat{v}_{i,\mathrm{B}}\right) n_j^{\mathrm{e}}\,\mathrm{d}^2\mathbf{x} + \oint_{\partial V^{\cap}} \left(\widehat{v}_{i,\mathrm{A}}\,\widehat{\tau}_{ij,\mathrm{B}} - \widehat{\tau}_{ij,\mathrm{A}}\,\widehat{v}_{i,\mathrm{B}}\right) n_j^{\mathrm{e}}\,\mathrm{d}^2\mathbf{x},\end{aligned} \tag{5}$$

where $\tau_{ij}(\mathbf{x},\omega)$ and $v_i(\mathbf{x},\omega)$, respectively, are the components of the stress tensor and particle velocity vector with subscripts A and B again denoting two independent elastodynamic states; $f_i(\mathbf{x},\omega)$ denotes the external volume force density; and $h_{ij}(\mathbf{x},\omega)$ represents the external deformation rate density source types. Domain $V^{\mathrm{e}}$ represents an arbitrary elastic spatial region enclosed by boundaries $\partial V^{\mathrm{e}}$ and $\partial V^{\cap}$ with an outward-pointing normal vector $\mathbf{n}^{\mathrm{e}} = n_j^{\mathrm{e}} = [n_1^{\mathrm{e}}, n_2^{\mathrm{e}}, n_3^{\mathrm{e}}]$, where the superscript $^{\mathrm{e}}$ denotes a quantity defined in the elastic solid. Boundary $\partial V^{\cap}$ again represents the common coupled interface between acoustic and elastic domains $\partial V^{\mathrm{a}}$ and $\partial V^{\mathrm{e}}$.

Eq. (5) represents the elastodynamic reciprocity theorem of the convolution type. The associated field and source quantities—$\widehat{\tau}_{ij}(\mathbf{x},\omega)$, $\widehat{v}_i(\mathbf{x},\omega)$, $\widehat{h}_{ij}(\mathbf{x},\omega)$, and $\widehat{f}_i(\mathbf{x},\omega)$—satisfy the space-frequency domain elastic wave equations forming a coupled, first-order system in a lossless, arbitrarily inhomogeneous anisotropic elastic medium

$$\jmath\omega\rho^{\mathrm{e}}\widehat{v}_i - \partial_j\widehat{\tau}_{ij} = \widehat{f}_i, \tag{6}$$

and

$$-\jmath\omega s^{\mathrm{e}}_{ijkl}\widehat{\tau}_{kl}+\frac{1}{2}\left(\partial_i\widehat{v}_j+\partial_j\widehat{v}_i\right)=\widehat{h}_{ij}, \tag{7}$$

where $\rho^{\mathrm{e}}=\rho^{\mathrm{e}}(\mathbf{x})$ and $s^{\mathrm{e}}_{ijkl}=s^{\mathrm{e}}_{ijkl}(\mathbf{x})$ are the density and compliance of the elastic medium, respectively.

### 2.3 Interface boundary considerations

Applying the boundary conditions that couple the elastic and acoustic domains at the interface $\partial V^{\cap}$ requires enforcing the continuity of traction and the normal component of the particle velocity. The continuity of traction at the acoustic–elastic interface $\partial V^{\cap}$ is given by:

$$-\widehat{p}=\widehat{t}_{\mathrm{n}}, \tag{8}$$

whereas

$$\widehat{t}_{\mathrm{u}}=\widehat{t}_{\mathrm{v}}=0, \tag{9}$$

because an inviscid fluid cannot support shear stress. Here, $\widehat{t}_{\mathrm{n}}$ represents the normal traction, $\widehat{t}_{\mathrm{u}}$ and $\widehat{t}_{\mathrm{v}}$ represent shear tractions, and the stresses and tractions are related by $\widehat{t}_i=\widehat{\tau}_{ij}n_j$, where $i,j\in\{u,v,n\}$. The continuity of the normal component of the particle velocity is expressed as

$$\widehat{v}^{a}_{\mathrm{n}}=\widehat{v}^{e}_{\mathrm{n}}. \tag{10}$$

In eq. (10), $\widehat{v}^{a}_{\mathrm{n}}$ and $\widehat{v}^{\mathrm{e}}_{\mathrm{n}}$ are the normal particle velocity components in the acoustic and the elastic solid, respectively, at any point on $\partial V^{\cap}$. The normal vector $n$ is relative to a locally orthogonal coordinate system, where the $uv$-plane is locally tangential to that point on the interface $\partial V^{\cap}$ (see Fig. 1).

By virtue of eq. (9), two terms on the right-hand side of eq. (5), $\widehat{v}_{i,\mathrm{A}}\widehat{\tau}_{ij,\mathrm{B}}\,n^{\mathrm{e}}_j$ and $\widehat{\tau}_{ij,\mathrm{A}}\widehat{v}_{i,\mathrm{B}}\,n^{\mathrm{e}}_j$ respectively become $\widehat{v}_{\mathrm{n,A}}\widehat{t}_{\mathrm{n,B}}$ and $\widehat{t}_{n,A}\,\widehat{v}_{n,B}$, reducing the reciprocity relation to

$$\begin{aligned}&\int_{V^{\mathrm{e}}}\left(-\widehat{\tau}_{ij,\mathrm{A}}\,\widehat{h}_{ij,\mathrm{B}}-\widehat{v}_{i,\mathrm{A}}\,\widehat{f}_{i,\mathrm{B}}+\widehat{h}_{ij,\mathrm{A}}\,\widehat{\tau}_{ij,\mathrm{B}}+\widehat{f}_{i,\mathrm{A}}\,\widehat{v}_{i,\mathrm{B}}\right)\mathrm{d}^3\mathbf{x}\\&=\oint_{\partial V^{\mathrm{e}}}\left(\widehat{v}_{i,\mathrm{A}}\,\widehat{\tau}_{ij,\mathrm{B}}-\widehat{\tau}_{ij,\mathrm{A}}\,\widehat{v}_{i,\mathrm{B}}\right)n^{\mathrm{e}}_j\,\mathrm{d}^2\mathbf{x}+\oint_{\partial V^{\cap}}\left(\widehat{v}_{n,\mathrm{A}}\,\widehat{t}_{n,\mathrm{B}}-\widehat{t}_{n,\mathrm{A}}\,\widehat{v}_{n,\mathrm{B}}\right)\mathrm{d}^2\mathbf{x}.\end{aligned} \tag{11}$$

Using eqs (8) and (10), and the fact that the normals defined on opposite sides of the interface $\partial V^{\cap}$ must satisfy $\mathbf{n}^{\mathrm{e}}=-\mathbf{n}^{\mathrm{a}}$, we rewrite eq. (1) as:

$$\begin{aligned}&\int_{V^{\mathrm{a}}}\left(\widehat{p}_{\mathrm{A}}\widehat{q}_{\mathrm{B}}-\widehat{v}_{i,\mathrm{A}}\,\widehat{f}_{i,\mathrm{B}}-\widehat{q}_{\mathrm{A}}\,\widehat{p}_{\mathrm{B}}+\widehat{f}_{i,\mathrm{A}}\,\widehat{v}_{i,\mathrm{B}}\right)\mathrm{d}^3\mathbf{x}\\&=\oint_{\partial V^{\mathrm{a}}}\left(\widehat{p}_{\mathrm{A}}\,\widehat{v}_{i,\mathrm{B}}-\widehat{v}_{i,\mathrm{A}}\,\widehat{p}_{\mathrm{B}}\right)n^{\mathrm{a}}_i\,\mathrm{d}^2\mathbf{x}-\oint_{\partial V^{\cap}}\left(\widehat{v}_{n,\mathrm{A}}\,\widehat{t}_{n,\mathrm{B}}-\widehat{t}_{n,\mathrm{A}}\,\widehat{v}_{n,\mathrm{B}}\right)\mathrm{d}^2\mathbf{x}.\end{aligned} \tag{12}$$

Adding eqs (11) and (12) yields

$$\begin{aligned}&\int_{V^{\mathrm{a}}}\left(\widehat{p}_{\mathrm{A}}\,\widehat{q}_{\mathrm{B}}-\widehat{v}_{i,\mathrm{A}}\,\widehat{f}_{i,\mathrm{B}}-\widehat{q}_{\mathrm{A}}\,\widehat{p}_{\mathrm{B}}+\widehat{f}_{i,\mathrm{A}}\,\widehat{v}_{i,\mathrm{B}}\right)\mathrm{d}^3\mathbf{x}\\&+\int_{V^{\mathrm{e}}}\left(-\widehat{\tau}_{ij,\mathrm{A}}\,\widehat{h}_{ij,\mathrm{B}}-\widehat{v}_{i,\mathrm{A}}\,\widehat{f}_{i,\mathrm{B}}+\widehat{h}_{ij,\mathrm{A}}\,\widehat{\tau}_{ij,\mathrm{B}}+\widehat{f}_{i,\mathrm{A}}\,\widehat{v}_{i,\mathrm{B}}\right)\mathrm{d}^3\mathbf{x}\\&=\oint_{\partial V^{\mathrm{a}}}\left(\widehat{p}_{\mathrm{A}}\,\widehat{v}_{i,\mathrm{B}}-\widehat{v}_{i,\mathrm{A}}\,\widehat{p}_{\mathrm{B}}\right)n^{\mathrm{a}}_i\,\mathrm{d}^2\mathbf{x}+\oint_{\partial V^{\mathrm{e}}}\left(\widehat{v}_{i,\mathrm{A}}\,\widehat{\tau}_{ij,\mathrm{B}}-\widehat{\tau}_{ij,\mathrm{A}}\,\widehat{v}_{i,\mathrm{B}}\right)n^{\mathrm{e}}_j\,\mathrm{d}^2\mathbf{x}.\end{aligned} \tag{13}$$

Eq. (13) represents the convolution-type reciprocity for a coupled acoustic–elastic system. A similar reciprocity relation to eq. (13) is given in de Hoop (1990).

Because the acoustic and elastic media are assumed to be lossless, the principle of time-reversal invariance (Bojarski 1983) can be applied to both domains. In the frequency domain, time reversal is replaced by complex conjugation, which is denoted by the $^*$ symbol over the field quantities. Time-reversal invariance states that if $\widehat{p}$ and $\widehat{v}_i$ are solutions to the acoustic wave-equation system in eqs (3) and (4) with source terms $\widehat{f}_i$ and $\widehat{q}$, then $\widehat{p}^{\,*}$ and $-\widehat{v}^{\,*}_i$ will satisfy the same equations with source terms $\widehat{f}^{\,*}_i$ and $-\widehat{q}^{\,*}$. Similarly, when $\widehat{\tau}_{ij}$ and $\widehat{v}_i$ are solutions to the elastic wave-equation system in eqs (6) and (7) with source terms $\widehat{f}_i$ and $\widehat{h}_{ij}$, then $\widehat{\tau}^{\,*}_{ij}$ and $-\widehat{v}^{\,*}_i$ will obey the same equations with source terms $\widehat{f}^{\,*}_i$ and $-\widehat{h}^{\,*}_{ij}$.

Enforcing time reversal for state A in eq. (13) leads to

$$\begin{aligned}&\int_{V^{\mathrm{a}}}\left(\widehat{p}^{\,*}_{\mathrm{A}}\widehat{q}_{\mathrm{B}}+\widehat{v}^{\,*}_{i,\mathrm{A}}\,\widehat{f}_{i,\mathrm{B}}+\widehat{q}^{\,*}_{\mathrm{A}}\,\widehat{p}_{\mathrm{B}}+\widehat{f}^{\,*}_{i,\mathrm{A}}\,\widehat{v}_{i,\mathrm{B}}\right)\mathrm{d}^3\mathbf{x}\\&+\int_{V^{\mathrm{e}}}\left(-\widehat{\tau}^{\,*}_{ij,\mathrm{A}}\,\widehat{h}_{ij,\mathrm{B}}+\widehat{v}^{\,*}_{i,\mathrm{A}}\,\widehat{f}_{i,\mathrm{B}}-\widehat{h}^{\,*}_{ij,\mathrm{A}}\,\widehat{\tau}_{ij,\mathrm{B}}+\widehat{f}^{\,*}_{i,\mathrm{A}}\,\widehat{v}_{i,\mathrm{B}}\right)\mathrm{d}^3\mathbf{x}\\&=\oint_{\partial V^{\mathrm{a}}}\left(\widehat{p}^{\,*}_{\mathrm{A}}\,\widehat{v}_{i,\mathrm{B}}+\widehat{v}^{\,*}_{i,\mathrm{A}}\,\widehat{p}_{\mathrm{B}}\right)n^{\mathrm{a}}_i\,\mathrm{d}^2\mathbf{x}-\oint_{\partial V^{\mathrm{e}}}\left(\widehat{v}^{\,*}_{i,\mathrm{A}}\,\widehat{\tau}_{ij,\mathrm{B}}+\widehat{\tau}^{\,*}_{ij,\mathrm{A}}\,\widehat{v}_{i,\mathrm{B}}\right)n^{\mathrm{e}}_j\,\mathrm{d}^2\mathbf{x}.\end{aligned} \tag{14}$$

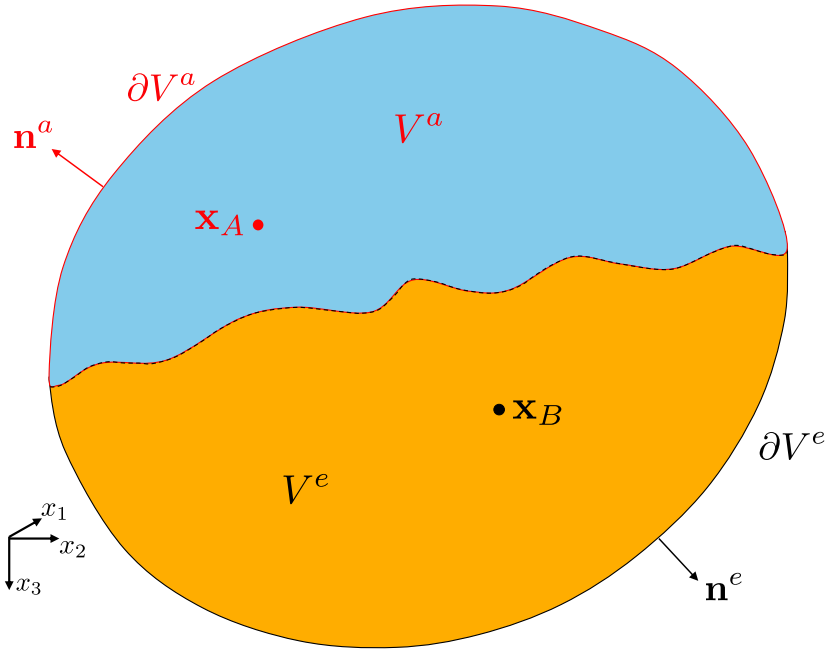


**Figure 2.** Configuration for coupled source–receiver reciprocity relations derived in Section 3.1. Points $\mathbf{x}_\mathrm{A}$ and $\mathbf{x}_\mathrm{B}$ are respectively located in the acoustic ($V^\mathrm{a}$) and elastic ($V^\mathrm{e}$) medium.

Eq. (14) represents the correlation-type reciprocity for a coupled acoustic–elastic system, because frequency-domain products (e.g. $\widehat{p}^{\,*}_\mathrm{A}\,\widehat{v}_{i,\mathrm{B}}$) correspond to time-domain correlations. Finally, in both the coupled convolution and correlation-type reciprocity theorems above, the medium properties in states $A$ and $B$ are assumed to be identical.

## 3 COUPLED ACOUSTIC–ELASTIC DOMAIN's GREEN's FUNCTION REPRESENTATIONS

In this section, we first derive the source–receiver reciprocity relations for the coupled acoustic–elastic system by substituting Green's functions for the wavefields in the convolution-type reciprocity relation (eq. 13). We then derive the coupled-domain Green's function representations using the correlation-type reciprocity relation (eq. 14). These representations form the foundation for SI in physically coupled acoustic–elastic systems, such as those found in exploration OBN settings. We consider a domain $V = V^\mathrm{a} \cup V^\mathrm{e}$ (see Fig. 1). Boundaries $\partial V^\mathrm{a}$ and $\partial V^\mathrm{e}$ do not necessarily coincide with physical boundaries; however, they must be continuous on the $\partial V^\cap$ interface.

### 3.1 Source–receiver reciprocity relations in coupled acoustic–elastic domain

We consider two cases involving two impulsive point sources: one located in the acoustic medium in state A, and the other in the solid in state B. In each case, $\mathbf{x}_\mathrm{A}$ is in the acoustic medium $V^\mathrm{a}$ and $\mathbf{x}_\mathrm{B}$ is in the solid medium $V^\mathrm{e}$ (see Fig. 2). Table 1 summarizes these two cases and the chosen source type.

Case 1 represents scenarios where only impulsive point sources of volume injection rate $\widehat{q}\,(\mathbf{x}, \omega)$ at point $\mathbf{x}_\mathrm{A}$ in $V^\mathrm{a}$ in state A and impulsive point force sources $\widehat{f}_i\,(\mathbf{x}, \omega)$ at point $\mathbf{x}_\mathrm{B}$ in $V^\mathrm{e}$ in state B are present. In this case, the coupled convolution-type reciprocity relation (eq. 13) simplifies to

$$
\begin{aligned}
&-\int_{V^\mathrm{a}} \widehat{q}_\mathrm{A}\,\widehat{p}_\mathrm{B}\,\mathrm{d}^3\mathbf{x} - \int_{V^\mathrm{e}} \widehat{v}_{i,\mathrm{A}}\,\widehat{f}_{i,\mathrm{B}}\,\mathrm{d}^3\mathbf{x} \\
&= \oint_{\partial V^\mathrm{a}} \left(\widehat{p}_\mathrm{A}\,\widehat{v}_{i,\mathrm{B}} - \widehat{v}_{i,\mathrm{A}}\widehat{p}_\mathrm{B}\right) n_i^\mathrm{a}\,\mathrm{d}^2\mathbf{x} + \oint_{\partial V^\mathrm{e}} \left(\widehat{v}_{i,\mathrm{A}}\,\widehat{\tau}_{ij,\mathrm{B}} - \widehat{\tau}_{ij,\mathrm{A}}\,\widehat{v}_{i,\mathrm{B}}\right) n_j^\mathrm{e}\,\mathrm{d}^2\mathbf{x}. \qquad (15)
\end{aligned}
$$

For an unbounded medium, we can consider the surface of integration $\partial V^\mathrm{a}$ and $\partial V^\mathrm{e}$ as a spherical arc with infinite radius $r \to \infty$. In this case, the contributions from the boundary integrals over $\partial V^\mathrm{a}$ and $\partial V^\mathrm{e}$ vanish, as they will be of order $O(r^{-1})$. Because the right-hand side of eq. (15) vanishes on both $\partial V^\mathrm{a}$ and $\partial V^\mathrm{e}$, the result is independent of the specific choice of boundaries $\partial V^\mathrm{a}$ and $\partial V^\mathrm{e}$, provided points $\mathbf{x}_\mathrm{A}$ and $\mathbf{x}_\mathrm{B}$ are contained within $\partial V^\mathrm{a} \cup \partial V^\mathrm{e}$. This further simplifies eq. (15) to

$$
\int_{V^\mathrm{a}} \widehat{q}_\mathrm{A}\,\widehat{p}_\mathrm{B}\,\mathrm{d}^3\mathbf{x} = -\int_{V^\mathrm{e}} \widehat{v}_{i,\mathrm{A}}\,\widehat{f}_{i,\mathrm{B}}\,\mathrm{d}^3\mathbf{x}. \qquad (16)
$$

**Table 1.** Summary of different source configurations in states A and B used in the coupled convolution-type reciprocity theorem for deriving coupled source–receiver reciprocity expressions.

| Case | State A ($\mathbf{x}_A$ in $V^a$) | State B ($\mathbf{x}_B$ in $V^e$) |
|---|---|---|
| 1 | $\widehat{q}_A = \delta(\mathbf{x}-\mathbf{x}_A), \quad \widehat{f}_{i,A} = 0$ | $\widehat{h}_{ij,B} = 0, \quad \widehat{f}_{i,B} = \delta(\mathbf{x}-\mathbf{x}_B)\delta_{il}$ |
| 2 | $\widehat{q}_A = \delta(\mathbf{x}-\mathbf{x}_A), \quad \widehat{f}_{i,A} = 0$ | $\widehat{h}_{ij,B} = \delta(\mathbf{x}-\mathbf{x}_B)\delta_{ir}\delta_{js}, \quad \widehat{f}_{i,B} = 0$ |

Table 1 presents the Case 1 source definitions found in eq. (16):

$$\widehat{q}_A(\mathbf{x},\omega) = \delta(\mathbf{x}-\mathbf{x}_A) \tag{17}$$

and

$$\widehat{f}_{i,B}(\mathbf{x},\omega) = \delta(\mathbf{x}-\mathbf{x}_B)\delta_{il}, \tag{18}$$

where $\delta(\mathbf{x})$ is the Dirac delta function and $\delta_{il}$ is the Kronecker delta function. The wavefields in states $A$ and $B$, needed in eq. (16) due to above sources, can be expressed in terms of impulse responses (i.e. acoustic and elastodynamic Green's functions):

$$\widehat{p}_B(\mathbf{x},\omega) = \widehat{G}^{p,f}_{,l}(\mathbf{x},\mathbf{x}_B,\omega) \tag{19}$$

and

$$\widehat{v}_{i,A}(\mathbf{x},\omega) = \widehat{G}^{v,q}_{i}(\mathbf{x},\mathbf{x}_A,\omega)\,. \tag{20}$$

Here, the Green's function notation $\widehat{G}^{v,q}_{i}(\mathbf{x},\mathbf{x}_A,\omega)$ represents the impulse response observed at $\mathbf{x}$ due to a source at $\mathbf{x}_A$. The double superscripts ($v$, $q$ here) respectively represent the observed field quantity (here particle velocity $v$) and the applied source (here impulsive point sources of volume injection rate $q$). If the observed field quantity or source is a vector or tensor, its component or direction is indicated by the subscripts. In this case, subscript $i$ denotes the $i$-th component of the observed particle velocity $v$. No subscript is required for scalar $q$ quantity. A circumflex accent on $\widehat{G}$ denotes the Fourier transform of causal time-domain Green's function $G^{v,q}_{i}(\mathbf{x},\mathbf{x}_A,t)$.

Substituting eqs (17)–(20) into eq. (16) and using the sifting property of the delta function leads to a source–receiver reciprocity relation for the coupled acoustic–elastic system:

$$\widehat{G}^{p,f}_{,l}(\mathbf{x}_A,\mathbf{x}_B,\omega) = -\widehat{G}^{v,q}_{l}(\mathbf{x}_B,\mathbf{x}_A,\omega)\,. \tag{21}$$

The Green's function $\widehat{G}^{v,q}_{l}(\mathbf{x}_B,\mathbf{x}_A,\omega)$ on the right-hand side of the above equation denotes the $l$-th component of particle velocity recorded at receiver location $\mathbf{x}_B$ within the elastic medium $V^e$, in response to a point impulsive volume injection rate source located at $\mathbf{x}_A$ in the acoustic medium $V^a$. In contrast, the Green's function $\widehat{G}^{p,f}_{,l}(\mathbf{x}_A,\mathbf{x}_B,\omega)$ on the left-hand side corresponds to the pressure field measured at a receiver positioned at $\mathbf{x}_A$ in the acoustic medium $V^a$, due to an impulsive point force applied in the $l$-th direction at $\mathbf{x}_B$ in the elastic medium $V^e$. Eq. (21) represents the source–receiver reciprocity for an OBN acquisition scenario where the airgun sources or ambient sources acting as volume injection rate sources are present anywhere above the seabed (i.e. in the water column), while the receivers are located just below the seabed (i.e. in the elastic solid).

Similarly, Case 2 is a scenario where we replace the source in eq. (18) by a point impulsive source of external deformation rate density $\widehat{h}_{ij}(\mathbf{x},\omega)$ defined as

$$\widehat{h}_{ij,B}(\mathbf{x},\omega) = \delta(\mathbf{x}-\mathbf{x}_B)\delta_{ir}\delta_{js}, \tag{22}$$

where the other sources remain the same as Case 1. Table 1 presents this Case 2 source definitions. Here, the coupled convolution-type reciprocity relation (eq. 13) simplifies to

$$\int_{V^a} \widehat{q}_A\,\widehat{p}_B\,\mathrm{d}^3\mathbf{x} = -\int_{V^e} \widehat{\tau}_{ij,A}\,\widehat{h}_{ij,B}\,\mathrm{d}^3\mathbf{x}. \tag{23}$$

We may express the wavefields needed in the above equation due to sources in Case 2 (Table 1) as

$$\widehat{p}_B(\mathbf{x},\omega) = \widehat{G}^{p,h}_{,rs}(\mathbf{x},\mathbf{x}_B,\omega) \tag{24}$$

and

$$\widehat{\tau}_{ij,A}(\mathbf{x},\omega) = \widehat{G}^{\tau,q}_{ij}(\mathbf{x},\mathbf{x}_A,\omega). \tag{25}$$

Substituting eqs (17), (22), (24) and (25) into eq. (23) and using the sifting property of the delta function yields the following coupled source–receiver reciprocity relation

$$\widehat{G}^{p,h}_{,rs}(\mathbf{x}_A,\mathbf{x}_B,\omega) = -\widehat{G}^{\tau,q}_{rs}(\mathbf{x}_B,\mathbf{x}_A,\omega). \tag{26}$$

For sources and receivers both located either in acoustic or elastic-solid media, the source–receiver reciprocity remains as presented in Wapenaar & Fokkema (2006). When both the source and receiver are in water and only impulsive point sources of volume injection rate $q$ are acting in both states, reciprocity is given by

$$\widehat{G}^{p,q}(\mathbf{x}_B,\mathbf{x}_A,\omega) = \widehat{G}^{p,q}(\mathbf{x}_A,\mathbf{x}_B,\omega). \tag{27}$$

When both the source and receiver are in solid media, three scenarios must be addressed. First, for cases where impulsive point sources of force $f$ are acting in both states, the reciprocity relation is

$$\widehat{G}^{v,f}_{m,n}(\mathbf{x}_\mathrm{B}, \mathbf{x}_\mathrm{A}, \omega) = \widehat{G}^{v,f}_{n,m}(\mathbf{x}_\mathrm{A}, \mathbf{x}_\mathrm{B}, \omega). \tag{28}$$

Second, when impulsive point sources of force $f$ act in state A and point sources of deformation type $h$ act in state B, the reciprocity relation

$$\widehat{G}^{\tau,f}_{qr,m}(\mathbf{x}_\mathrm{B}, \mathbf{x}_\mathrm{A}, \omega) = \widehat{G}^{v,h}_{m,qr}(\mathbf{x}_\mathrm{A}, \mathbf{x}_\mathrm{B}, \omega). \tag{29}$$

Third, when point sources of deformation type $h$ are acting in both states, the reciprocity relation is

$$\widehat{G}^{\tau,h}_{qr,mn}(\mathbf{x}_\mathrm{B}, \mathbf{x}_\mathrm{A}, \omega) = \widehat{G}^{\tau,h}_{mn,qr}(\mathbf{x}_\mathrm{A}, \mathbf{x}_\mathrm{B}, \omega). \tag{30}$$

### 3.2 Pressure-type Green's function expression for seismic interferometry in coupled acoustic–elastic media

As with the coupled source–receiver reciprocity relations derived earlier, one can make specific choices regarding the wavefields and source fields in states A and B to derive the pressure Green's function representation for SI. In this section, we examine various cases for the locations of points $\mathbf{x}_\mathrm{A}$ and $\mathbf{x}_\mathrm{B}$ inside $\partial V^\mathrm{a} \cup \partial V^\mathrm{e}$ and define the corresponding sources and wavefields to derive the expression for the pressure-type Green's functions using the correlation-type coupled reciprocity relation derived in eq. (14).

#### *3.2.1 Points $\mathbf{x}_\mathrm{A}$ and $\mathbf{x}_\mathrm{B}$ in acoustic media $V^\mathrm{a}$*

For the scenario where points $\mathbf{x}_\mathrm{A}$ and $\mathbf{x}_\mathrm{B}$ are located in acoustic medium $V^\mathrm{a}$, one need only consider impulsive point sources of volume injection-rate density $\widehat{q}\,(\mathbf{x}, \omega)$ defined by

$$\widehat{q}_\chi(\mathbf{x}, \omega) = \delta(\mathbf{x} - \mathbf{x}_\chi) \quad \text{for} \quad \chi = A, B, \tag{31}$$

while the external forces $\widehat{f}(\mathbf{x}, \omega)$ in $V^\mathrm{a}$ are assumed to be zero in both states. There are no sources in $V^\mathrm{e}$ for states A and B. In this scenario, the correlation-type coupled reciprocity relation given in eq. (14) simplifies to

$$\begin{aligned}&\int_{V^\mathrm{a}} \left(\widehat{p}^{\,*}_\mathrm{A}\, \widehat{q}_\mathrm{B} + \widehat{q}^{\,*}_\mathrm{A}\, \widehat{p}_\mathrm{B}\right) \mathrm{d}^3\mathbf{x} \\ &= \oint_{\partial V^\mathrm{a}} \left(\widehat{p}^{\,*}_\mathrm{A}\, \widehat{v}_{i,\mathrm{B}} + \widehat{v}^{\,*}_{i,\mathrm{A}}\, \widehat{p}_\mathrm{B}\right) n^\mathrm{a}_i \, \mathrm{d}^2\mathbf{x} - \oint_{\partial V^\mathrm{e}} \left(\widehat{v}^{\,*}_{i,\mathrm{A}}\, \widehat{\tau}_{ij,\mathrm{B}} + \widehat{\tau}^{\,*}_{ij,\mathrm{A}}\, \widehat{v}_{i,\mathrm{B}}\right) n^\mathrm{e}_j \, \mathrm{d}^2\mathbf{x}.\end{aligned} \tag{32}$$

We define the recorded pressure wavefield $\widehat{p}(\mathbf{x}, \omega)$ at $\mathbf{x}$ in $V^\mathrm{a}$ for both the states as the observed impulse responses (Green's functions), given by:

$$\widehat{p}_\chi(\mathbf{x}, \omega) = \widehat{G}^{p,q}(\mathbf{x}, \mathbf{x}_\chi, \omega) \quad \text{for} \quad \chi = A, B. \tag{33}$$

We then obtain the expressions for the particle velocities observed at $\mathbf{x}$ in $V^\mathrm{a}$ for both the states by substituting eq. (33) and $\widehat{f}_\mathrm{A}(\mathbf{x}, \omega) = \widehat{f}_\mathrm{B}(\mathbf{x}, \omega) = 0$ into the acoustic wave eq. (3) as:

$$\widehat{v}_{i,\chi}(\mathbf{x}, \omega) = \frac{-1}{\jmath\omega\rho^\mathrm{a}(\mathbf{x})} \partial_i \widehat{G}^{p,q}(\mathbf{x}, \mathbf{x}_\chi, \omega) \quad \text{for} \quad \chi = A, B. \tag{34}$$

For the stress and velocity wavefields recorded at $\mathbf{x}$ in $V^\mathrm{e}$ for both states, we define the stress and velocity Green's functions due to the sources in eq. (31) as

$$\widehat{\tau}_{ij,\chi}(\mathbf{x}, \omega) = \widehat{G}^{\tau,q}_{ij}(\mathbf{x}, \mathbf{x}_\chi, \omega) \quad \text{for} \quad \chi = A, B, \tag{35}$$

and

$$\widehat{v}_{i,\chi}(\mathbf{x}, \omega) = \widehat{G}^{v,q}_{i}(\mathbf{x}, \mathbf{x}_\chi, \omega) \quad \text{for} \quad \chi = A, B. \tag{36}$$

Table 2 summarizes the sources along with the corresponding wavefields in $V^\mathrm{a}$ and $V^\mathrm{e}$ for both states.

Substituting eqs (31), (33)–(36) into eq. (32) and applying the sifting property of the Dirac delta function obtains

$$\begin{aligned}&\widehat{G}^{p,q*}(\mathbf{x}_\mathrm{B}, \mathbf{x}_\mathrm{A}, \omega) + \widehat{G}^{p,q}(\mathbf{x}_\mathrm{A}, \mathbf{x}_\mathrm{B}, \omega) \\ &= \oint_{\partial V^\mathrm{a}} \frac{-1}{\jmath\omega\rho^\mathrm{a}(\mathbf{x})} \left(\widehat{G}^{p,q*}(\mathbf{x}, \mathbf{x}_\mathrm{A}, \omega)\, \partial_i \widehat{G}^{p,q}(\mathbf{x}, \mathbf{x}_\mathrm{B}, \omega) - \partial_i \widehat{G}^{p,q*}(\mathbf{x}, \mathbf{x}_\mathrm{A}, \omega)\, \widehat{G}^{p,q}(\mathbf{x}, \mathbf{x}_\mathrm{B}, \omega)\right) n^\mathrm{a}_i \, \mathrm{d}^2\mathbf{x} \\ &- \oint_{\partial V^\mathrm{e}} \left(\widehat{G}^{v,q*}_i(\mathbf{x}, \mathbf{x}_\mathrm{A}, \omega)\, \widehat{G}^{\tau,q}_{ij}(\mathbf{x}, \mathbf{x}_\mathrm{B}, \omega) + \widehat{G}^{\tau,q*}_{ij}(\mathbf{x}, \mathbf{x}_\mathrm{A}, \omega)\, \widehat{G}^{v,q}_i(\mathbf{x}, \mathbf{x}_\mathrm{B}, \omega)\right) n^\mathrm{e}_j \, \mathrm{d}^2\mathbf{x}.\end{aligned} \tag{37}$$

**Table 2.** Choice of sources and wavefields in $V^{\mathrm{a}}$ and $V^{\mathrm{e}}$ in states A and B, when points $\mathbf{x}_{\mathrm{A}}$ and $\mathbf{x}_{\mathrm{B}}$ are in $V^{\mathrm{a}}$, to be used in the coupled convolution-type reciprocity theorem to derive pressure Green's function expression.

| Domain | Parameter | State A | State B |
|---|---|---|---|
| in $V^{\mathrm{a}}$ | $\widehat{q}(\mathbf{x},\omega)$ | $\delta(\mathbf{x}-\mathbf{x}_{\mathrm{A}})$ | $\delta(\mathbf{x}-\mathbf{x}_{\mathrm{B}})$ |
| | $\widehat{f}_i(\mathbf{x},\omega)$ | 0 | 0 |
| | $\widehat{p}(\mathbf{x},\omega)$ | $\widehat{G}^{p,q}(\mathbf{x},\mathbf{x}_{\mathrm{A}},\omega)$ | $\widehat{G}^{p,q}(\mathbf{x},\mathbf{x}_{\mathrm{B}},\omega)$ |
| | $\widehat{v}_i(\mathbf{x},\omega)$ | $\frac{1}{\jmath\omega\rho^{\mathrm{a}}(\mathbf{x})}\partial_i\widehat{G}^{p,q}(\mathbf{x},\mathbf{x}_{\mathrm{A}},\omega)$ | $\frac{1}{\jmath\omega\rho^{\mathrm{a}}(\mathbf{x})}\partial_i\widehat{G}^{p,q}(\mathbf{x},\mathbf{x}_{\mathrm{B}},\omega)$ |
| in $V^{\mathrm{e}}$ | $\widehat{h}_{ij}(\mathbf{x},\omega)$ | 0 | 0 |
| | $\widehat{f}_i(\mathbf{x},\omega)$ | 0 | 0 |
| | $\widehat{\tau}_{ij}(\mathbf{x},\omega)$ | $\widehat{G}^{\tau,q}_{ij}(\mathbf{x},\mathbf{x}_{\mathrm{A}},\omega)$ | $\widehat{G}^{\tau,q}_{ij}(\mathbf{x},\mathbf{x}_{\mathrm{B}},\omega)$ |
| | $\widehat{v}_i(\mathbf{x},\omega)$ | $\widehat{G}^{v,q}_{i}(\mathbf{x},\mathbf{x}_{\mathrm{A}},\omega)$ | $\widehat{G}^{v,q}_{i}(\mathbf{x},\mathbf{x}_{\mathrm{B}},\omega)$ |

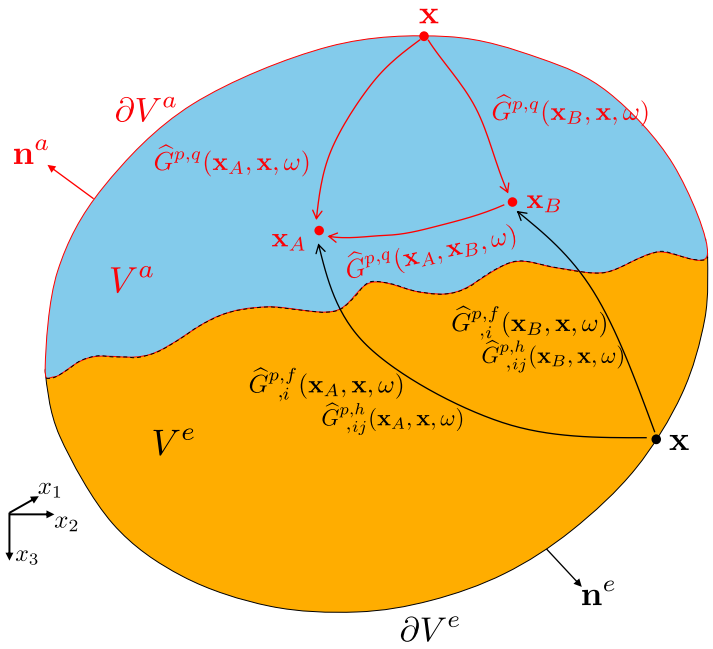


**Figure 3.** Seismic interferometry by cross-correlation for the pressure-type Green's function representation when receivers are in $V^{\mathrm{a}}$. Green's function $\widehat{G}^{p,q}(\mathbf{x}_{\mathrm{A}},\mathbf{x}_{\mathrm{B}},\omega)$ can be obtained by cross-correlating the observations at $\mathbf{x}_{\mathrm{A}}$ and $\mathbf{x}_{\mathrm{B}}$, and integrating along the source coordinate $\mathbf{x}$ at $\partial V^{\mathrm{a}}$ and $\partial V^{\mathrm{e}}$ (eq. 38). The figure shows the wavefields observed at $\mathbf{x}_{\mathrm{A}}$ and $\mathbf{x}_{\mathrm{B}}$ along with the corresponding sources required at $\mathbf{x}$ on $\partial V^{\mathrm{a}}$ and $\partial V^{\mathrm{e}}$ for pressure Green's function retrieval. Note that the rays represent the full responses between the source and receiver points, including primary and multiple scattering mode conversions due to inhomogeneities inside and outside the region $\partial V^{\mathrm{a}}\cup\partial V^{\mathrm{e}}$.

Applying source–receiver reciprocity from eqs (21)–(27) into both sides of the above results in

$$
\begin{aligned}
&2\ \Re\left\{\widehat{G}^{p,q}(\mathbf{x}_{\mathrm{A}},\mathbf{x}_{\mathrm{B}},\omega)\right\}\\
&=\oint_{\partial V^{\mathrm{a}}}\frac{-1}{\jmath\omega\rho^{\mathrm{a}}(\mathbf{x})}\left(\widehat{G}^{p,q*}(\mathbf{x}_{\mathrm{A}},\mathbf{x},\omega)\,\partial_i\widehat{G}^{p,q}(\mathbf{x}_{\mathrm{B}},\mathbf{x},\omega)-\partial_i\widehat{G}^{p,q*}(\mathbf{x}_{\mathrm{A}},\mathbf{x},\omega)\,\widehat{G}^{p,q}(\mathbf{x}_{\mathrm{B}},\mathbf{x},\omega)\right)n_i^{\mathrm{a}}\mathrm{d}^2\mathbf{x}\\
&-\oint_{\partial V^{\mathrm{e}}}\left(\widehat{G}^{p,f*}_{,i}(\mathbf{x}_{\mathrm{A}},\mathbf{x},\omega)\,\widehat{G}^{p,h}_{,ij}(\mathbf{x}_{\mathrm{B}},\mathbf{x},\omega)+(\widehat{G}^{p,h*}_{,ij}(\mathbf{x}_{\mathrm{A}},\mathbf{x},\omega)\,\widehat{G}^{p,f}_{,i}(\mathbf{x}_{\mathrm{B}},\mathbf{x},\omega)\right)n_j^{\mathrm{e}}\mathrm{d}^2\mathbf{x}.
\end{aligned}
\tag{38}
$$

where the $\Re$ operator extracts the real part of a complex argument.

In the time domain, the products on the right-hand side of the above equation (e.g. $\widehat{G}^{p,q*}\,\partial_i\widehat{G}^{p,q}$) correspond to cross-correlations, while the left-hand side represents the pressure Green's function and its time-reversed counterpart [i.e. $G^{p,q}(\mathbf{x}_{\mathrm{A}},\mathbf{x}_{\mathrm{B}},t)+G^{p,q}(\mathbf{x}_{\mathrm{A}},\mathbf{x}_{\mathrm{B}},-t)$]. The term $\widehat{G}^{p,q}$ under the acoustic-surface integral $\oint_{\partial V^{\mathrm{a}}}$ denotes the response of the volume injection-rate density sources $q$ at $\mathbf{x}$ on $\partial V^{\mathrm{a}}$. Similarly, the terms $\widehat{G}^{p,f}$ and $\widehat{G}^{p,h}$ under the elastic-surface integral $\oint_{\partial V^{\mathrm{e}}}$ respectively represent the responses of force sources $f$ and deformation sources $h$ at $\mathbf{x}$ on $\partial V^{\mathrm{e}}$. Integration in both integrals is performed along the source coordinate $\mathbf{x}$ (see Fig. 3).

The exact relationship expressed in eq. (38) provides a means to retrieve the complete pressure Green's function $\widehat{G}^{p,q}(\mathbf{x}_{\mathrm{A}},\mathbf{x}_{\mathrm{B}},\omega)$ using cross-correlations of observed Green's functions from sources on $\partial V^{\mathrm{a}}$ and $\partial V^{\mathrm{e}}$ (Fig. 3). This formulation applies to any lossless, arbitrary, inhomogeneous, anisotropic, coupled acoustic–elastic medium and forms the basis for acoustic SI when receivers are located within the acoustic medium. The retrieved Green's function is complete, containing all arrivals—direct and scattered—including primaries, multiples and mode conversions from inhomogeneities both within and outside the boundaries $\partial V^{\mathrm{a}}$ and $\partial V^{\mathrm{e}}$.

Although eq. (38) is an exact representation of the acoustic Green's function, it is impractical for field data applications in its current form due to its complexity. Specifically, one must evaluate the superposition of two correlation products under both integrals, $\oint_{\partial V^{\mathrm{a}}}$ and $\oint_{\partial V^{\mathrm{e}}}$. Furthermore, monopole $\widehat{G}^{p,q}$ as well as dipole responses $\partial_i \widehat{G}^{p,q}$ are required for all source positions $\mathbf{x}$ on $V^{\mathrm{a}}$. Similarly, two different types of sources, $\widehat{f}(\mathbf{x}, \omega)$ and $\widehat{h}(\mathbf{x}, \omega)$, are required for all source positions $\mathbf{x}$ on $V^{\mathrm{e}}$. To overcome these challenges, we develop practical approximations for both integrals.

*3.2.1.1 Simplification of the acoustic boundary integral (eq. 38)* When the wavefield on the boundary $\partial V^{\mathrm{a}}$ in eq. (37) satisfies outgoing (i.e. radiation or absorbing) boundary conditions such that the outward-propagating wavefield at the $\partial V^{\mathrm{a}}$ boundary does not return after being scattered by external inhomogeneities, Wapenaar & Fokkema (2006) demonstrates that the acoustic boundary integral can be approximated as:

$$\text{Acoustic Boundary Integral} \approx \frac{2}{\rho^{\mathrm{a}} c^{\mathrm{a}}} \oint_{\partial V^{\mathrm{a}}} \widehat{G}^{p,q*}(\mathbf{x}_{\mathrm{A}}, \mathbf{x}, \omega)\, \widehat{G}^{p,q}(\mathbf{x}_{\mathrm{B}}, \mathbf{x}, \omega)\, \mathrm{d}^2\mathbf{x}, \tag{39}$$

where the acoustic medium at and outside $\partial V^{\mathrm{a}}$ is assumed to be homogeneous with a propagation velocity $c^{\mathrm{a}}$ and mass density $\rho^{\mathrm{a}}$.

*3.2.1.2 Simplification of the elastic boundary integrand (eq. 38)* To approximate the contribution of sources on the elastic boundary $\partial V^{\mathrm{e}}$ to the acoustic Green's function $2\,\Re\{\widehat{G}^{p,q}(\mathbf{x}_{\mathrm{A}}, \mathbf{x}_{\mathrm{B}}, \omega)\}$ in eq. (38), we can follow the procedure developed in Wapenaar & Fokkema (2006) starting with eq. (A-8) found therein. This simplification involves decomposing the wavefield at the $\partial V^{\mathrm{e}}$ boundary in eq. (37) into inward- and outward-propagating components and assuming that the medium outside the domain is isotropic and homogeneous, ensuring the absence of cross-terms between inwards and outwards propagating waves. The complete argument is thoroughly developed in Wapenaar & Haimé (1990). Accordingly, we assume the elastic medium at and outside $\partial V^{\mathrm{e}}$ to be homogeneous, isotropic, and source-free, with mass density $\rho^{\mathrm{e}}$, and $P$- and $S$-wave velocities $c_P$ and $c_S$. The elastic boundary integral term in the convolution-type reciprocity relation (eq. 14) can then be expressed as (see eq. A-8 in Wapenaar & Fokkema (2006)):

$$-\oint_{\partial V^{\mathrm{e}}} \left(\widehat{v}^{*}_{i,\mathrm{A}}\, \widehat{\tau}_{ij,\mathrm{B}} + \widehat{\tau}^{*}_{ij,\mathrm{A}}\, \widehat{v}_{i,\mathrm{B}}\right) n^{\mathrm{e}}_j\, \mathrm{d}^2\mathbf{x} \approx \frac{2}{\jmath\omega\rho^{\mathrm{e}}} \oint_{\partial V^{\mathrm{e}}} \left((\partial_j \widehat{\Phi}^{*}_{\mathrm{A}})\, \widehat{\Phi}_{\mathrm{B}} + (\partial_j \widehat{\Psi}^{*}_{k,\mathrm{A}})\, \widehat{\Psi}_{k,\mathrm{B}}\right) n^{\mathrm{e}}_j\, \mathrm{d}^2\mathbf{x}, \tag{40}$$

where $\widehat{\Phi}$ and $\widehat{\Psi}_k$ respectively represent the observed $P$- and $S$-wave potentials at $\mathbf{x}$ on $\partial V^{\mathrm{e}}$ with subscripts A and B correspond to states A and B. These potentials satisfy the Helmholtz equations (Aki & Richards 2002).

In the current case (Case 1 in Table 2), points $\mathbf{x}_{\mathrm{A}}$ and $\mathbf{x}_{\mathrm{B}}$ are located above the seafloor, and we have chosen impulsive point sources with volume injection-rate density $\widehat{q}(\mathbf{x}, \omega)$ at points $\mathbf{x}_{\mathrm{A}}$ in state A and at $\mathbf{x}_{\mathrm{B}}$ in state B. For $\mathbf{x}$ in $V^{\mathrm{e}}$, the velocity and stresses in both the states due to above sources at $\mathbf{x}_{\mathrm{A}}$ and $\mathbf{x}_{\mathrm{B}}$ are expressed in terms of coupled Green's functions as given in eqs (35) and (36). For $\mathbf{x}$ at or outside $\partial V^{\mathrm{e}}$ but still in elastic medium, we express the $P$- and $S$-wave potentials in states A and B in terms of Green's functions as

$$\widehat{\Phi}_{\chi}(\mathbf{x}, \omega) = \widehat{G}^{\phi,q}_0(\mathbf{x}, \mathbf{x}_{\chi}, \omega) \quad \text{for} \quad \chi = A, B \tag{41}$$

and

$$\widehat{\Psi}_{k,\chi}(\mathbf{x}, \omega) = \widehat{G}^{\phi,q}_k(\mathbf{x}, \mathbf{x}_{\chi}, \omega) \quad \text{for} \quad \chi = A, B, \tag{42}$$

where the superscript $\phi$ denotes that the observed wavefield quantity at $\mathbf{x}$ is a $P$- or $S$-wave potential. To describe both wave types with a single Green's function, we use subscript $K$ that takes on values 0, 1, 2 and 3. Hence, in $\widehat{G}^{\phi,q}_K(\mathbf{x}, \mathbf{x}_{\mathrm{B}}, \omega)$, the observed wavefield at $\mathbf{x}$ is a $P$ wave for $K = 0$ or an $S$-wave component for $K = k = 1, 2, 3$. Substituting eqs (35), (36), (41) and (42) into eq. (40) gives

$$\begin{aligned} &-\oint_{\partial V^{\mathrm{e}}} \left(\widehat{G}^{v,q*}_i(\mathbf{x}, \mathbf{x}_{\mathrm{A}}, \omega)\widehat{G}^{\tau,q}_{ij}(\mathbf{x}, \mathbf{x}_{\mathrm{B}}, \omega) + \widehat{G}^{\tau,q*}_{ij}(\mathbf{x}, \mathbf{x}_{\mathrm{A}}, \omega)\widehat{G}^{v,q}_i(\mathbf{x}, \mathbf{x}_{\mathrm{B}}, \omega)\right) n^{\mathrm{e}}_j\, \mathrm{d}^2\mathbf{x} \\ &\approx \frac{2}{\jmath\omega\rho^{\mathrm{e}}} \oint_{\partial V^{\mathrm{e}}} \partial_j \widehat{G}^{\phi,q*}_K(\mathbf{x}, \mathbf{x}_{\mathrm{A}}, \omega)\, \widehat{G}^{\phi,q}_K(\mathbf{x}, \mathbf{x}_{\mathrm{B}}, \omega)\, n^{\mathrm{e}}_j\, \mathrm{d}^2\mathbf{x}. \end{aligned} \tag{43}$$

Applying source–receiver reciprocity from eqs (21) and (26) to the left side of the above results in

$$\begin{aligned} &-\oint_{\partial V^{\mathrm{e}}} \left(\widehat{G}^{p,f*}_{,i}(\mathbf{x}_{\mathrm{A}}, \mathbf{x}, \omega)\, \widehat{G}^{p,h}_{,ij}(\mathbf{x}_{\mathrm{B}}, \mathbf{x}, \omega) + (\widehat{G}^{p,h*}_{,ij}(\mathbf{x}_{\mathrm{A}}, \mathbf{x}, \omega)\, \widehat{G}^{p,f}_{,i}(\mathbf{x}_{\mathrm{B}}, \mathbf{x}, \omega)\right) n^{\mathrm{e}}_j \mathrm{d}^2\mathbf{x} \\ &\approx \frac{2}{\jmath\omega\rho^{\mathrm{e}}} \oint_{\partial V^{\mathrm{e}}} \partial_j \widehat{G}^{\phi,q*}_K(\mathbf{x}, \mathbf{x}_{\mathrm{A}}, \omega)\, \widehat{G}^{\phi,q}_K(\mathbf{x}, \mathbf{x}_{\mathrm{B}}, \omega)\, n^{\mathrm{e}}_j\, \mathrm{d}^2\mathbf{x}. \end{aligned} \tag{44}$$

Note that the repeated subscript $K$ now represents a summation from 0 to 3, accounting for the different wave types in eq. (40), and that the left-hand side is the elastic boundary integral from eq. (38). Let us examine the source–receiver reciprocity for the Green's function $\widehat{G}^{\phi,q}_K(\mathbf{x}, \mathbf{x}_{\mathrm{A}}, \omega)$, where $\mathbf{x}$ lies in the solid and $\mathbf{x}_{\mathrm{A}}$ is in the water. In this case (refer to Table 1, Case 1 for the source configuration), we can write the source–receiver reciprocity relation (eq. 21) as

$$\widehat{G}^{p,f}_{,l}(\mathbf{x}_{\mathrm{A}}, \mathbf{x}, \omega) = -\widehat{G}^{v,q}_l(\mathbf{x}, \mathbf{x}_{\mathrm{A}}, \omega)\,. \tag{45}$$

Alternatively, if the source $\widehat{f}(\mathbf{x}, \omega)$ is replaced with impulsive *P*- and *S*-wave point sources (Wapenaar & Berkhout 1989) at $\mathbf{x}$, we can define another coupled source–receiver reciprocity as:

$$\widehat{G}^{p,\phi}_{,K}(\mathbf{x}_\mathrm{A}, \mathbf{x}, \omega) = -\widehat{G}^{\phi,q}_{K}(\mathbf{x}, \mathbf{x}_\mathrm{A}, \omega)\,. \tag{46}$$

In this case, the superscript $\phi$ in $\widehat{G}^{p,\phi}_{,K}(\mathbf{x}_\mathrm{A}, \mathbf{x}, \omega)$ indicates a *P*-wave source for $K = 0$ or a vector-polarized *S*-wave source for $K = k = 1, 2, 3$. Accordingly, in $\widehat{G}^{\phi,q}_{K}(\mathbf{x}, \mathbf{x}_\mathrm{A}, \omega)$, the observed wave potential at $\mathbf{x}$ is the *P*-wave potential for $K = 0$, and the *S*-wave potential for $K = k = 1, 2, 3$. Introducing the above reciprocity relation in eq. (43) results in

$$\text{Elastic Boundary Integral} \approx \tfrac{2}{J\omega\rho^\mathrm{e}} \oint_{\partial V^\mathrm{e}} \partial_j \widehat{G}^{p,\phi*}_{,K}(\mathbf{x}_\mathrm{A}, \mathbf{x}, \omega)\, \widehat{G}^{p,\phi}_{,K}(\mathbf{x}_\mathrm{B}, \mathbf{x}, \omega)\, n^\mathrm{e}_j \,\mathrm{d}^2\mathbf{x}. \tag{47}$$

Despite its simple form, the above equation requires the availability of monopole and dipole responses, $\widehat{G}^{p,\phi}$ and $\partial_i \widehat{G}^{p,\phi}_{,K}$, from *P*- and *S*-wave sources at $\mathbf{x}$. Assuming as previously that the elastic medium at and outside $\partial V^\mathrm{e}$ is homogeneous with mass density $\rho^\mathrm{e}$ and *P*- and *S*-wave velocities $c^P$ and $c^S$, respectively, the dipole response can be approximated in terms of a monopole response (Wapenaar & Fokkema 2006) as

$$\partial_j \widehat{G}^{p,\phi}_{,K}(\mathbf{x}_\mathrm{A}, \mathbf{x}, \omega)\, n^\mathrm{e}_j \approx \frac{\omega}{Jc^K} \widehat{G}^{p,\phi}_{,K}(\mathbf{x}_\mathrm{A}, \mathbf{x}, \omega), \tag{48}$$

where

$$c^K = \begin{cases} c^P & \text{for } K = 0 \\ c^S & \text{for } K = k = 1, 2, 3. \end{cases} \tag{49}$$

Note that since $K$ does not appear as a subscript in $c^K$, no summation takes place over $K$ on the right-hand side of eq. (48). Using the dipole approximation from eq. (48) in eq. (47), the elastic boundary integral reduces to:

$$\text{Elastic Boundary Integral} \approx \tfrac{2}{\rho^\mathrm{e} c^K} \oint_{\partial V^\mathrm{e}} \widehat{G}^{p,\phi*}_{,K}(\mathbf{x}_\mathrm{A}, \mathbf{x}, \omega)\, \widehat{G}^{p,\phi}_{,K}(\mathbf{x}_\mathrm{B}, \mathbf{x}, \omega)\, \mathrm{d}^2\mathbf{x}. \tag{50}$$

Using the acoustic and elastic boundary integral approximations (eqs 39 and 50), the pressure Green's function in eq. (38) approximates to:

$$\begin{aligned} &\Re\left\{\widehat{G}^{p,q}(\mathbf{x}_\mathrm{A}, \mathbf{x}_\mathrm{B}, \omega)\right\} \\ &\approx \frac{1}{\rho^\mathrm{a} c^\mathrm{a}} \oint_{\partial V^\mathrm{a}} \widehat{G}^{p,q*}(\mathbf{x}_\mathrm{A}, \mathbf{x}, \omega)\, \widehat{G}^{p,q}(\mathbf{x}_\mathrm{B}, \mathbf{x}, \omega)\, \mathrm{d}^2\mathbf{x} \\ &+ \frac{1}{\rho^\mathrm{e} c^K} \oint_{\partial V^\mathrm{e}} \widehat{G}^{p,\phi*}_{,K}(\mathbf{x}_\mathrm{A}, \mathbf{x}, \omega)\, \widehat{G}^{p,\phi}_{,K}(\mathbf{x}_\mathrm{B}, \mathbf{x}, \omega)\, \mathrm{d}^2\mathbf{x}. \end{aligned} \tag{51}$$

This approximation is highly accurate when $\partial V^\mathrm{a}$ and $\partial V^\mathrm{e}$ are part of a sphere with a sufficiently large radius such that all rays are normal to $\partial V^\mathrm{a}$ and $\partial V^\mathrm{e}$; otherwise, it may introduce significant amplitude errors. Additionally, events that would be otherwise completely cancelled when using eq. (38) may instead give rise to artifacts due to incomplete destructive interference. Nonetheless, the application of eq. (51) will correctly retrieve the phases of all arrivals.

It is important to note that the Green's function retrieved under the aforementioned approximations represents only the high-frequency propagating component of the wavefield, rather than the complete broad-band response. As demonstrated by Zheng (2010) and Zheng *et al.* (2011), the far-field approximation can be removed by invoking the exact boundary integral equation method, and the exact, full-frequency bandwidth Green's function can be retrieved-including all scattering effects-provided that the source locations are known, as is the case for active-source experiments. Although, unlike the far-field approximation, which requires cross-correlating wavefields observed at $\mathbf{x}_\mathrm{A}$ and $\mathbf{x}_\mathrm{B}$ from a common source at $\mathbf{x} \in \partial V^\mathrm{a} \cup \partial V^\mathrm{e}$, the exact method requires correlations between receiver pairs for each source as well as between distinct source locations. For applications using ambient sources, this exact Green's function retrieval technique remains applicable as long as the ambient source distribution can be reasonably estimated.

### 3.2.2 *Points* $\mathbf{x}_\mathrm{A}$ *and* $\mathbf{x}_\mathrm{B}$ *in the solid media* $V^\mathrm{e}$

When both points are located beneath the seafloor, we place impulsive point sources of the external deformation rate density $\widehat{h}_{ij}(\mathbf{x}, \omega)$ at $\mathbf{x}_\mathrm{A}$ and $\mathbf{x}_\mathrm{B}$ within $V^\mathrm{e}$, with all other sources set to zero. Table 3 summarizes these sources and the resulting wavefields in both $V^\mathrm{a}$ and $V^\mathrm{e}$ for the two states. Substituting the parameters from Table 3 into the reciprocity relation in eq. (14) and using the Dirac delta function sifting property yields:

$$\begin{aligned} &\left(\widehat{G}^{\tau,h*}_{rs,mn}(\mathbf{x}_\mathrm{B}, \mathbf{x}_\mathrm{A}, \omega) + \widehat{G}^{\tau,h}_{mn,rs}(\mathbf{x}_\mathrm{A}, \mathbf{x}_\mathrm{B}, \omega)\right) \\ &= \oint_{\partial V^\mathrm{a}} \frac{1}{J\omega\rho^\mathrm{a}(\mathbf{x})} \left(\widehat{G}^{p,h*}_{,mn}(\mathbf{x}, \mathbf{x}_\mathrm{A}, \omega)\, \partial_i \widehat{G}^{p,h}_{,rs}(\mathbf{x}, \mathbf{x}_\mathrm{B}, \omega) - \partial_i \widehat{G}^{p,h*}_{,mn}(\mathbf{x}, \mathbf{x}_\mathrm{A}, \omega)\, \widehat{G}^{p,h}_{,rs}(\mathbf{x}, \mathbf{x}_\mathrm{B}, \omega)\right) n^\mathrm{a}_i \mathrm{d}^2\mathbf{x} \\ &+ \oint_{\partial V^\mathrm{e}} \left(\widehat{G}^{v,h*}_{i,mn}(\mathbf{x}, \mathbf{x}_\mathrm{A}, \omega)\, \widehat{G}^{\tau,h}_{ij,rs}(\mathbf{x}, \mathbf{x}_\mathrm{B}, \omega) + \widehat{G}^{\tau,h*}_{ij,mn}(\mathbf{x}, \mathbf{x}_\mathrm{A}, \omega)\, \widehat{G}^{v,h}_{i,rs}(\mathbf{x}, \mathbf{x}_\mathrm{B}, \omega)\right) n^\mathrm{e}_j \mathrm{d}^2\mathbf{x}. \end{aligned} \tag{52}$$

**Table 3.** Summary of sources and wavefields in states A and B, used for the pressure Green's function expression when points $\mathbf{x}_A$ and $\mathbf{x}_B$ are in $V^e$.

| Domain | Parameter | State A | State B |
|---|---|---|---|
| in $V^a$ | $\widehat{q}(\mathbf{x},\omega)$ | 0 | 0 |
| | $\widehat{f}_i(\mathbf{x},\omega)$ | 0 | 0 |
| | $\widehat{p}(\mathbf{x},\omega)$ | $\widehat{G}^{p,h}_{,mn}(\mathbf{x},\mathbf{x}_A,\omega)$ | $\widehat{G}^{p,h}_{,rs}(\mathbf{x},\mathbf{x}_B,\omega)$ |
| | $\widehat{v}_i(\mathbf{x},\omega)$ | $\frac{J}{\omega\rho^a(\mathbf{x})}\partial_i\widehat{G}^{p,h}_{,mn}(\mathbf{x},\mathbf{x}_A,\omega)$ | $\frac{J}{\omega\rho^a(\mathbf{x})}\partial_i\widehat{G}^{p,h}_{,rs}(\mathbf{x},\mathbf{x}_B,\omega)$ |
| in $V^e$ | $\widehat{h}_{ij}(\mathbf{x},\omega)$ | $\delta(\mathbf{x}-\mathbf{x}_A)\,\delta_{im}\delta_{jn}$ | $\delta(\mathbf{x}-\mathbf{x}_B)\,\delta_{ir}\delta_{js}$ |
| | $\widehat{f}_i(\mathbf{x},\omega)$ | 0 | 0 |
| | $\widehat{\tau}_{ij}(\mathbf{x},\omega)$ | $\widehat{G}^{\tau,h}_{ij,mn}(\mathbf{x},\mathbf{x}_A,\omega)$ | $\widehat{G}^{\tau,h}_{ij,rs}(\mathbf{x},\mathbf{x}_B,\omega)$ |
| | $\widehat{v}_i(\mathbf{x},\omega)$ | $\widehat{G}^{v,h}_{i,mn}(\mathbf{x},\mathbf{x}_A,\omega)$ | $\widehat{G}^{\tau,h}_{i,rs}(\mathbf{x},\mathbf{x}_B,\omega)$ |

In Table 3, consider external deformation rate density source tensors $\widehat{h}_{ij}(\mathbf{x},\omega)=\delta(\mathbf{x}-\mathbf{x}_A)\delta_{im}\delta_{jn}$ in state A and $\widehat{h}_{ij}(\mathbf{x},\omega)=\delta(\mathbf{x}-\mathbf{x}_B)\delta_{ir}\delta_{js}$ in state B, both located within $V^e$. If we consider only their normal components and sum eq. (52) over all such sources, we can write

$$\begin{aligned}
&\sum_{m=n=1}^{3}\sum_{r=s=1}^{3}\left(\widehat{G}^{\tau,h*}_{rs,mn}(\mathbf{x}_B,\mathbf{x}_A,\omega)+\widehat{G}^{\tau,h}_{mn,rs}(\mathbf{x}_A,\mathbf{x}_B,\omega)\right)\\
&\quad=\sum_{m=n=1}^{3}\sum_{r=s=1}^{3}\left\{\oint_{\partial V^a}\frac{1}{J\omega\rho^a(\mathbf{x})}\left(\widehat{G}^{p,h*}_{,mn}(\mathbf{x},\mathbf{x}_A,\omega)\,\partial_i\widehat{G}^{p,h}_{,rs}(\mathbf{x},\mathbf{x}_B,\omega)-\partial_i\widehat{G}^{p,h*}_{,mn}(\mathbf{x},\mathbf{x}_A,\omega)\,\widehat{G}^{p,h}_{,rs}(\mathbf{x},\mathbf{x}_B,\omega)\right)n_i^a\mathrm{d}^2\mathbf{x}\right.\\
&\quad\left.+\oint_{\partial V^e}\left(\widehat{G}^{v,h*}_{i,mn}(\mathbf{x},\mathbf{x}_A,\omega)\,\widehat{G}^{\tau,h}_{ij,rs}(\mathbf{x},\mathbf{x}_B,\omega)+\widehat{G}^{\tau,h*}_{ij,mn}(\mathbf{x},\mathbf{x}_A,\omega)\,\widehat{G}^{v,h}_{i,rs}(\mathbf{x},\mathbf{x}_B,\omega)\right)n_j^e\mathrm{d}^2\mathbf{x}\right\},
\end{aligned}\tag{53}$$

or using repeated subscripts

$$\begin{aligned}
&\left(\widehat{G}^{\tau,h*}_{rr,mm}(\mathbf{x}_B,\mathbf{x}_A,\omega)+\widehat{G}^{\tau,h}_{mm,rr}(\mathbf{x}_A,\mathbf{x}_B,\omega)\right)\\
&=\oint_{\partial V^a}\frac{1}{J\omega\rho^a(\mathbf{x})}\left(\widehat{G}^{p,h*}_{,mm}(\mathbf{x},\mathbf{x}_A,\omega)\,\partial_i\widehat{G}^{p,h}_{,rr}(\mathbf{x},\mathbf{x}_B,\omega)-\partial_i\widehat{G}^{p,h*}_{,mm}(\mathbf{x},\mathbf{x}_A,\omega)\,\widehat{G}^{p,h}_{,rr}(\mathbf{x},\mathbf{x}_B,\omega)\right)n_i^a\mathrm{d}^2\mathbf{x}\\
&+\oint_{\partial V^e}\left(\widehat{G}^{v,h*}_{i,mm}(\mathbf{x},\mathbf{x}_A,\omega)\,\widehat{G}^{\tau,h}_{ij,rr}(\mathbf{x},\mathbf{x}_B,\omega)+\widehat{G}^{\tau,h*}_{ij,mm}(\mathbf{x},\mathbf{x}_A,\omega)\,\widehat{G}^{v,h}_{i,rr}(\mathbf{x},\mathbf{x}_B,\omega)\right)n_j^e\mathrm{d}^2\mathbf{x}.
\end{aligned}\tag{54}$$

Using the source–receiver reciprocity of eqs (26), (29) and (30) into the above equation results in

$$\begin{aligned}
&2\ \Re\left\{\widehat{G}^{\tau,h}_{mm,rr}(\mathbf{x}_A,\mathbf{x}_B,\omega)\right\}\\
&=\oint_{\partial V^a}\frac{1}{J\omega\rho^a(\mathbf{x})}\left(\widehat{G}^{\tau,q*}_{mm}(\mathbf{x}_A,\mathbf{x},\omega)\,\partial_i\widehat{G}^{\tau,q}_{rr}(\mathbf{x}_B,\mathbf{x},\omega)-\partial_i\widehat{G}^{\tau,q*}_{mm}(\mathbf{x}_A,\mathbf{x},\omega)\,\widehat{G}^{\tau,q}_{rr}(\mathbf{x}_B,\mathbf{x},\omega)\right)n_i^a\mathrm{d}^2\mathbf{x}\\
&+\oint_{\partial V^e}\left(\widehat{G}^{\tau,f*}_{mm,i}(\mathbf{x}_A,\mathbf{x},\omega)\,\widehat{G}^{\tau,h}_{rr,ij}(\mathbf{x}_B,\mathbf{x},\omega)+\widehat{G}^{\tau,h*}_{mm,ij}(\mathbf{x}_A,\mathbf{x},\omega)\,\widehat{G}^{\tau,f}_{rr,i}(\mathbf{x}_B,\mathbf{x},\omega)\right)n_j^e\mathrm{d}^2\mathbf{x}.
\end{aligned}\tag{55}$$

Assuming an isotropic elastic solid, we define pressure as the negative of one third of stress tensor trace (Bennethum 2006)

$$\widehat{p}^{\,e}=-\frac{1}{3}(\widehat{\tau}_{11}+\widehat{\tau}_{22}+\widehat{\tau}_{33}).\tag{56}$$

For a point composite source of volume injection rate type, defined as

$$\widehat{q}^{\,e}=\frac{1}{3}(\widehat{h}_{11}+\widehat{h}_{22}+\widehat{h}_{33}),\tag{57}$$

we write the pressure eq. (56) as

$$\begin{aligned}
\widehat{G}^{p^e,q^e}&=-\frac{1}{9}\left((\widehat{G}^{\tau,h}_{11,11}+\widehat{G}^{\tau,h}_{11,22}+\widehat{G}^{\tau,h}_{11,33})\right.\\
&\quad+(\widehat{G}^{\tau,h}_{22,11}+\widehat{G}^{\tau,h}_{22,22}+\widehat{G}^{\tau,h}_{22,33})\\
&\quad\left.+(\widehat{G}^{\tau h}_{33,11}+\widehat{G}^{\tau,h}_{33,22}+\widehat{G}^{\tau,h}_{33,33})\right)\\
&=-\frac{1}{9}\,\widehat{G}^{\tau,h}_{mm,rr}\,.
\end{aligned}\tag{58}$$

For point volume injection rate sources $q$, eq. (56) becomes

$$\begin{aligned}
\widehat{G}^{p^e,q}&=-\frac{1}{3}(\widehat{G}^{\tau,q}_{11}+\widehat{G}^{\tau,q}_{22}+\widehat{G}^{\tau,q}_{33})\\
&=-\frac{1}{3}\widehat{G}^{\tau,q}_{mm}\ \text{or}\ -\frac{1}{3}\widehat{G}^{\tau,q}_{rr}.
\end{aligned}\tag{59}$$

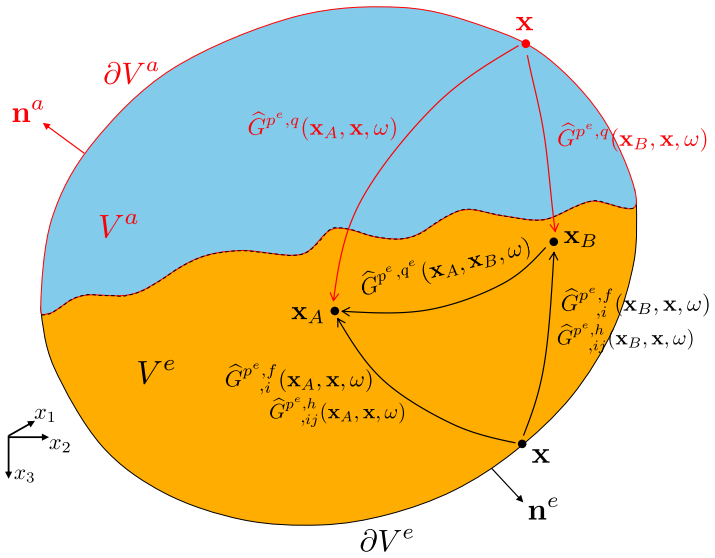


**Figure 4.** Pressure-type Green's function representation through interferometry when both the receivers are in $V^{\mathrm{e}}$. According to eq. (60), the Green's function $\widehat{G}^{p^{\mathrm{e}},q^{\mathrm{e}}}(\mathbf{x}_{\mathrm{A}},\mathbf{x}_{\mathrm{B}},\omega)$ can be obtained by cross-correlating the observations at $\mathbf{x}_{\mathrm{A}}$ and $\mathbf{x}_{\mathrm{B}}$, and integrating along the source coordinate $\mathbf{x}$ at $\partial V^{\mathrm{a}}$ and $\partial V^{\mathrm{e}}$. The wavefields observed at $\mathbf{x}_{\mathrm{A}}$ and $\mathbf{x}_{\mathrm{B}}$, along with the corresponding sources required at $\mathbf{x}$ on $\partial V^{\mathrm{a}}$ and $\partial V^{\mathrm{e}}$ for Green's function $\widehat{G}^{p^{\mathrm{e}},q^{\mathrm{e}}}(\mathbf{x}_{\mathrm{A}},\mathbf{x}_{\mathrm{B}},\omega)$ retrieval, are shown. Note that the rays in this figure represent the full responses between the source and receiver points, including primary and multiple scattering, as well as mode conversion due to inhomogeneities inside and outside the region $\partial V^{\mathrm{a}} \cup \partial V^{\mathrm{e}}$.

Similar expressions apply for point force sources $f$ and point stress sources $h_{ij}$ as well. Using these definitions, we rewrite eq. (55) as:

$$
\begin{aligned}
&2\ \Re\left\{\widehat{G}^{p^{\mathrm{e}},q^{\mathrm{e}}}(\mathbf{x}_{\mathrm{A}},\mathbf{x}_{\mathrm{B}},\omega)\right\}\\
&=\oint_{\partial V^{\mathrm{a}}}\frac{-1}{\jmath\omega\rho^{\mathrm{a}}(\mathbf{x})}\left(\widehat{G}^{p^{\mathrm{e}},q*}(\mathbf{x}_{\mathrm{A}},\mathbf{x},\omega)\,\partial_i\widehat{G}^{p^{\mathrm{e}},q}(\mathbf{x}_{\mathrm{B}},\mathbf{x},\omega)-\partial_i\widehat{G}^{p^{\mathrm{e}},q*}(\mathbf{x}_{\mathrm{A}},\mathbf{x},\omega)\,\widehat{G}^{p^{\mathrm{e}},q}(\mathbf{x}_{\mathrm{B}},\mathbf{x},\omega)\right)n_i^{\mathrm{a}}\mathrm{d}^2\mathbf{x}\\
&-\oint_{\partial V^{\mathrm{e}}}\left(\widehat{G}^{p^{\mathrm{e}},f*}_{\ \ ,i}(\mathbf{x}_{\mathrm{A}},\mathbf{x},\omega)\,\widehat{G}^{p^{\mathrm{e}},h}_{\ \ ,ij}(\mathbf{x}_{\mathrm{B}},\mathbf{x},\omega)+\widehat{G}^{p^{\mathrm{e}},h*}_{\ \ ,ij}(\mathbf{x}_{\mathrm{A}},\mathbf{x},\omega)\,\widehat{G}^{p^{\mathrm{e}},f}_{\ \ ,i}(\mathbf{x}_{\mathrm{B}},\mathbf{x},\omega)\right)n_j^{\mathrm{e}}\mathrm{d}^2\mathbf{x}.
\end{aligned}
\tag{60}
$$

Fig. 4 illustrates the Green's functions of the above equation observed at $\mathbf{x}_{\mathrm{A}}$ and $\mathbf{x}_{\mathrm{B}}$ and corresponding sources required at $\mathbf{x}$ on $\partial V^{\mathrm{a}}$ and $\partial V^{\mathrm{e}}$ to obtain the Green's function $\widehat{G}^{p^{\mathrm{e}},q^{\mathrm{e}}}(\mathbf{x}_{\mathrm{A}},\mathbf{x}_{\mathrm{B}},\omega)$.

Eq. (60) is identical to eq. (38), except that $\widehat{p}^{\,e}$ and $\widehat{q}^{\,e}$ in this context are defined for the elastodynamic state. Consequently, it can be approximated using a similar expression to eq. (51):

$$
\begin{aligned}
\Re\left\{\widehat{G}^{p^{\mathrm{e}},q^{\mathrm{e}}}(\mathbf{x}_{\mathrm{A}},\mathbf{x}_{\mathrm{B}},\omega)\right\}\approx&\frac{1}{\rho^{\mathrm{a}}c^{\mathrm{a}}}\oint_{\partial V^{\mathrm{a}}}\widehat{G}^{p^{\mathrm{e}},q*}(\mathbf{x}_{\mathrm{A}},\mathbf{x},\omega)\,\widehat{G}^{p^{\mathrm{e}},q}(\mathbf{x}_{\mathrm{B}},\mathbf{x},\omega)\,\mathrm{d}^2\mathbf{x}\\
&+\frac{1}{\rho^{\mathrm{e}}c^K}\oint_{\partial V^{\mathrm{e}}}\widehat{G}^{p^{\mathrm{e}},\phi*}_{\ \ ,K}(\mathbf{x}_{\mathrm{A}},\mathbf{x},\omega)\,\widehat{G}^{p^{\mathrm{e}},\phi}_{\ \ ,K}(\mathbf{x}_{\mathrm{B}},\mathbf{x},\omega)\,\mathrm{d}^2\mathbf{x},
\end{aligned}
\tag{61}
$$

where the superscripts $p$ and $q$ in the Green's functions on the left-hand side of eq. (38) are respectively replaced by the elastodynamic pressure and source, $\widehat{p}^{\,e}$ and $\widehat{q}^{\,e}$ as both $\mathbf{x}_{\mathrm{A}}$ and $\mathbf{x}_{\mathrm{B}}$ are located within the solid. Similarly, the superscript $p$ in the Green's functions on the right-hand side is replaced by $\widehat{p}^{\,e}$, reflecting that $\mathbf{x}_{\mathrm{A}}$ is within the solid medium.

### *3.2.3 Point $\mathbf{x}_{\mathrm{A}}$ in the acoustic media $V^{\mathrm{a}}$ and $\mathbf{x}_{\mathrm{B}}$ in the solid media $V^{\mathrm{e}}$*

We now consider impulsive point sources of volume injection-rate density $\widehat{q}\,(\mathbf{x},\omega)$ at point $\mathbf{x}_{\mathrm{A}}$ in $V^{\mathrm{a}}$ for state A, and point impulsive sources of external deformation rate density $\widehat{h}_{ij}(\mathbf{x},\omega)$ at $\mathbf{x}_{\mathrm{B}}$ in $V^{\mathrm{e}}$ for state B. Table 4 summarizes the sources and corresponding wavefields in $V^{\mathrm{a}}$ and $V^{\mathrm{e}}$ for both states. Substituting the parameters from Table 4 into the correlation-type reciprocity relation (14) results in:

$$
\begin{aligned}
&\widehat{G}^{p,h}_{\ \ ,rs}(\mathbf{x}_{\mathrm{A}},\mathbf{x}_{\mathrm{B}},\omega)-\widehat{G}^{\tau,q*}_{rs}(\mathbf{x}_{\mathrm{A}},\mathbf{x}_{\mathrm{B}},\omega)\\
&=\oint_{\partial V^{\mathrm{a}}}\frac{-1}{\jmath\omega\rho^{\mathrm{a}}(\mathbf{x})}\left(\widehat{G}^{p,q*}(\mathbf{x},\mathbf{x}_{\mathrm{A}},\omega)\,\partial_i\widehat{G}^{p,h}_{\ \ ,rs}(\mathbf{x},\mathbf{x}_{\mathrm{B}},\omega)-\partial_i\widehat{G}^{p,q*}(\mathbf{x},\mathbf{x}_{\mathrm{A}},\omega)\,\widehat{G}^{p,h}_{\ \ ,rs}(\mathbf{x},\mathbf{x}_{\mathrm{B}},\omega)\right)n_i^{\mathrm{a}}\mathrm{d}^2\mathbf{x}\\
&-\oint_{\partial V^{\mathrm{e}}}\left(\widehat{G}^{v,q*}_{i}(\mathbf{x},\mathbf{x}_{\mathrm{A}},\omega)\,\widehat{G}^{\tau,h}_{ij,rs}(\mathbf{x},\mathbf{x}_{\mathrm{B}},\omega)+\widehat{G}^{\tau,q*}_{ij}(\mathbf{x},\mathbf{x}_{\mathrm{A}},\omega)*\widehat{G}^{v,h}_{i,rs}(\mathbf{x},\mathbf{x}_{\mathrm{B}},\omega)\right)n_j^{\mathrm{e}}\mathrm{d}^2\mathbf{x}.
\end{aligned}
\tag{62}
$$

**Table 4.** Summary of sources and wavefields in states $A$ and $B$, used for the pressure Green's function expression when point $\mathbf{x}_\mathrm{A}$ is in $V^\mathrm{a}$, and point $\mathbf{x}_\mathrm{B}$ is in $V^\mathrm{e}$.

| Domain | Parameter | State A | State B |
|---|---|---|---|
| in $V^\mathrm{a}$ | $\widehat{q}(\mathbf{x},\omega)$ | $\delta(\mathbf{x}-\mathbf{x}_\mathrm{A})$ | 0 |
| | $\widehat{f}_i(\mathbf{x},\omega)$ | 0 | 0 |
| | $\widehat{p}(\mathbf{x},\omega)$ | $\widehat{G}^{p,q}(\mathbf{x},\mathbf{x}_\mathrm{A},\omega)$ | $\widehat{G}^{p,h}_{,rs}(\mathbf{x},\mathbf{x}_\mathrm{B},\omega)$ |
| | $\widehat{v}_i(\mathbf{x},\omega)$ | $\frac{1}{\jmath\omega\rho^\mathrm{a}(\mathbf{x})}\partial_i\widehat{G}^{p,q}(\mathbf{x},\mathbf{x}_\mathrm{A},\omega)$ | $\frac{1}{\jmath\omega\rho^\mathrm{a}(\mathbf{x})}\partial_i\widehat{G}^{p,h}_{,rs}(\mathbf{x},\mathbf{x}_\mathrm{B},\omega)$ |
| in $V^\mathrm{e}$ | $\widehat{h}_{ij}(\mathbf{x},\omega)$ | 0 | $\delta(\mathbf{x}-\mathbf{x}_\mathrm{B})\,\delta_{ir}\delta_{js}$ |
| | $\widehat{f}_i(\mathbf{x},\omega)$ | 0 | 0 |
| | $\widehat{\tau}_{ij}(\mathbf{x},\omega)$ | $\widehat{G}^{\tau,q}_{ij}(\mathbf{x},\mathbf{x}_\mathrm{A},\omega)$ | $\widehat{G}^{\tau,h}_{ij,rs}(\mathbf{x},\mathbf{x}_\mathrm{B},\omega)$ |
| | $\widehat{v}_i(\mathbf{x},\omega)$ | $\widehat{G}^{v,q}_{i}(\mathbf{x},\mathbf{x}_\mathrm{A},\omega)$ | $\widehat{G}^{v,h}_{i,rs}(\mathbf{x},\mathbf{x}_\mathrm{B},\omega)$ |

Similar to the previous section, in Table 4, we consider external deformation rate density source tensor $\widehat{h}_{ij}(\mathbf{x},\omega)=\delta(\mathbf{x}-\mathbf{x}_\mathrm{B})\delta_{ir}\delta_{js}$ in $V^\mathrm{e}$ for state B. If we consider only its normal components and sum eq. (62) over all such sources, we can write:

$$\begin{aligned}
&\sum_{r=s=1}^{3}\left(\widehat{G}^{p,h}_{,rs}(\mathbf{x}_\mathrm{A},\mathbf{x}_\mathrm{B},\omega)-\widehat{G}^{\tau,q*}_{rs}(\mathbf{x}_\mathrm{A},\mathbf{x}_\mathrm{B},\omega)\right)\\
&\quad=\sum_{r=s=1}^{3}\left\{\oint_{\partial V^\mathrm{a}}\frac{-1}{\jmath\omega\rho^\mathrm{a}(\mathbf{x})}\left(\widehat{G}^{p,q*}(\mathbf{x},\mathbf{x}_\mathrm{A},\omega)\,\partial_i\widehat{G}^{p,h}_{,rs}(\mathbf{x},\mathbf{x}_\mathrm{B},\omega)-\partial_i\widehat{G}^{p,q*}(\mathbf{x},\mathbf{x}_\mathrm{A},\omega)\,\widehat{G}^{p,h}_{,rs}(\mathbf{x},\mathbf{x}_\mathrm{B},\omega)\right)n^\mathrm{a}_i\mathrm{d}^2\mathbf{x}\right.\\
&\quad-\left.\oint_{\partial V^\mathrm{e}}\left(\widehat{G}^{v,q*}_{i}(\mathbf{x},\mathbf{x}_\mathrm{A},\omega)\,\widehat{G}^{\tau,h}_{ij,rs}(\mathbf{x},\mathbf{x}_\mathrm{B},\omega)+\widehat{G}^{\tau,q*}_{ij}(\mathbf{x},\mathbf{x}_\mathrm{A},\omega)*\widehat{G}^{v,h}_{i,rs}(\mathbf{x},\mathbf{x}_\mathrm{B},\omega)\right)n^\mathrm{e}_j\mathrm{d}^2\mathbf{x}\right\},
\end{aligned}\tag{63}$$

or using repeated subscripts

$$\begin{aligned}
&\widehat{G}^{p,h}_{,rr}(\mathbf{x}_\mathrm{A},\mathbf{x}_\mathrm{B},\omega)-\widehat{G}^{\tau,q*}_{rr}(\mathbf{x}_\mathrm{A},\mathbf{x}_\mathrm{B},\omega)\\
&\quad=\oint_{\partial V^\mathrm{a}}\frac{-1}{\jmath\omega\rho^\mathrm{a}(\mathbf{x})}\left(\widehat{G}^{p,q*}(\mathbf{x},\mathbf{x}_\mathrm{A},\omega)\,\partial_i\widehat{G}^{p,h}_{,rr}(\mathbf{x},\mathbf{x}_\mathrm{B},\omega)-\partial_i\widehat{G}^{p,q*}(\mathbf{x},\mathbf{x}_\mathrm{A},\omega)\,\widehat{G}^{p,h}_{,rr}(\mathbf{x},\mathbf{x}_\mathrm{B},\omega)\right)n^\mathrm{a}_i\mathrm{d}^2\mathbf{x}\\
&\quad-\oint_{\partial V^\mathrm{e}}\left(\widehat{G}^{v,q*}_{i}(\mathbf{x},\mathbf{x}_\mathrm{A},\omega)\,\widehat{G}^{\tau,h}_{ij,rr}(\mathbf{x},\mathbf{x}_\mathrm{B},\omega)+\widehat{G}^{\tau,q*}_{ij}(\mathbf{x},\mathbf{x}_\mathrm{A},\omega)*\widehat{G}^{v,h}_{i,rr}(\mathbf{x},\mathbf{x}_\mathrm{B},\omega)\right)n^\mathrm{e}_j\mathrm{d}^2\mathbf{x}.
\end{aligned}\tag{64}$$

Using the source–receiver reciprocity relations (21)–(27), (29) and (30) on both sides of the equations gives,

$$\begin{aligned}
&\widehat{G}^{p,h}_{,rr}(\mathbf{x}_\mathrm{A},\mathbf{x}_\mathrm{B},\omega)+\widehat{G}^{p,h*}_{,rr}(\mathbf{x}_\mathrm{A},\mathbf{x}_\mathrm{B},\omega)\\
&\quad=\oint_{\partial V^\mathrm{a}}\frac{1}{\jmath\omega\rho^\mathrm{a}(\mathbf{x})}\left(\widehat{G}^{p,q*}(\mathbf{x}_\mathrm{A},\mathbf{x},\omega)\,\partial_i\widehat{G}^{\tau,q}_{rr}(\mathbf{x}_\mathrm{B},\mathbf{x},\omega)-\partial_i\widehat{G}^{p,q*}(\mathbf{x}_\mathrm{A},\mathbf{x},\omega)\,\widehat{G}^{\tau,q}_{rr}(\mathbf{x}_\mathrm{B},\mathbf{x},\omega)\right)n^\mathrm{a}_i\mathrm{d}^2\mathbf{x}\\
&\quad+\oint_{\partial V^\mathrm{e}}\left(\widehat{G}^{p,f*}_{,i}(\mathbf{x}_\mathrm{A},\mathbf{x},\omega)\,\widehat{G}^{\tau,h}_{rr,ij}(\mathbf{x}_\mathrm{B},\mathbf{x},\omega)+\widehat{G}^{p,h*}_{,ij}(\mathbf{x}_\mathrm{A},\mathbf{x},\omega)\,\widehat{G}^{p,f}_{,i}(\mathbf{x}_\mathrm{B},\mathbf{x},\omega)\right)n^\mathrm{e}_j\mathrm{d}^2\mathbf{x}.
\end{aligned}\tag{65}$$

Applying summation notation and using the previously defined elastodynamic pressure $p^\mathrm{e}$ and its corresponding composite source $q^\mathrm{e}$ definitions at point $\mathbf{x}_\mathrm{B}$ yields,

$$\begin{aligned}
&2\ \Re\left\{\widehat{G}^{p,q^\mathrm{e}}(\mathbf{x}_\mathrm{A},\mathbf{x}_\mathrm{B},\omega)\right\}\\
&=\oint_{\partial V^\mathrm{a}}\frac{-1}{\jmath\omega\rho^\mathrm{a}(\mathbf{x})}\left(\widehat{G}^{p,q*}(\mathbf{x}_\mathrm{A},\mathbf{x},\omega)\,\partial_i\widehat{G}^{p^\mathrm{e},q}(\mathbf{x}_\mathrm{B},\mathbf{x},\omega)-\partial_i\widehat{G}^{p,q*}(\mathbf{x}_\mathrm{A},\mathbf{x},\omega)\,\widehat{G}^{p^\mathrm{e},q}(\mathbf{x}_\mathrm{B},\mathbf{x},\omega)\right)n^\mathrm{a}_i\,\mathrm{d}^2\mathbf{x}\\
&-\oint_{\partial V^\mathrm{e}}\left(\widehat{G}^{p,f*}_{,i}(\mathbf{x}_\mathrm{A},\mathbf{x},\omega)\,\widehat{G}^{p^\mathrm{e},h}_{,ij}(\mathbf{x}_\mathrm{B},\mathbf{x},\omega)+\widehat{G}^{p,h*}_{,ij}(\mathbf{x}_\mathrm{A},\mathbf{x},\omega)*\widehat{G}^{p^\mathrm{e},f}_{,i}(\mathbf{x}_\mathrm{B},\mathbf{x},\omega)\right)n^\mathrm{e}_j\,\mathrm{d}^2\mathbf{x}.
\end{aligned}\tag{66}$$

Fig. 5 illustrates the Green's functions of the above equation observed at $\mathbf{x}_\mathrm{A}$ and $\mathbf{x}_\mathrm{B}$, along with the corresponding sources required at $\mathbf{x}$ on $\partial V^\mathrm{a}$ and $\partial V^\mathrm{e}$ to obtain the Green's function $\widehat{G}^{p,q^\mathrm{e}}(\mathbf{x}_\mathrm{A},\mathbf{x}_\mathrm{B},\omega)$. This expression is analogous to eq. (38), except that $\widehat{p}^{\,e}$ and $\widehat{q}^{\,e}$ at point $\mathbf{x}_\mathrm{B}$ are defined for the elastodynamic state. An expression similar to eq. (51) can be written to approximate this Green's function, as was done in the previous section.

### 3.3 Velocity Green's function expression for seismic interferometry in coupled acoustic–elastic domain

To derive particle velocity Green's function expressions appropriate for SI, we keep points $\mathbf{x}_\mathrm{A}$ and $\mathbf{x}_\mathrm{B}$ in solid $V^\mathrm{e}$ (see Fig. 6) and choose impulsive point force sources $\widehat{f}(\mathbf{x},\omega)$ at both points; all other sources in $V^\mathrm{e}$ and $V^\mathrm{a}$ are set to zero. Table 5 summarizes the choice of sources along with the wavefields they generate in $V^\mathrm{a}$ and $V^\mathrm{e}$ for both states. Substituting parameters from Table 5 into the correlation-type reciprocity

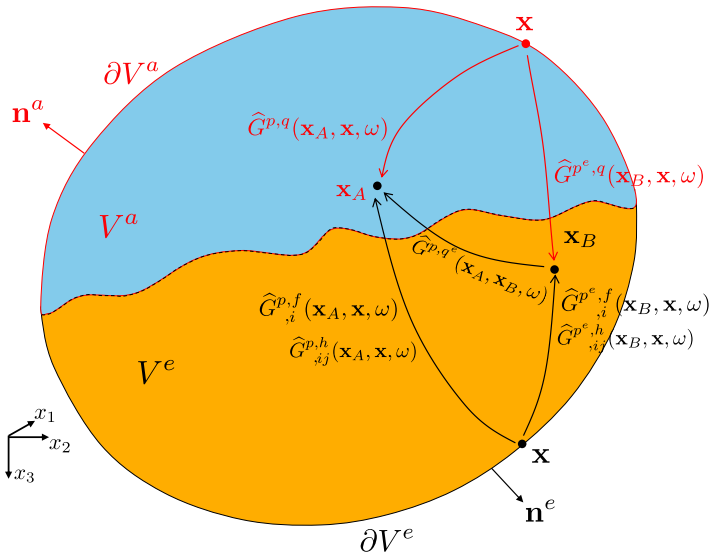


**Figure 5.** Pressure-type Green's function representation through interferometry when one receiver is in $V^{\mathrm{a}}$ and other in $V^{\mathrm{e}}$. According to eq. (66), the Green's function $\widehat{G}^{p,q^{\mathrm{e}}}(\mathbf{x}_{\mathrm{A}}, \mathbf{x}_{\mathrm{B}}, \omega)$ can be obtained by cross-correlating the observations at $\mathbf{x}_{\mathrm{A}}$ and $\mathbf{x}_{\mathrm{B}}$, and integrating along the source coordinate $\mathbf{x}$ at $\partial V^{\mathrm{a}}$ and $\partial V^{\mathrm{e}}$. The wavefields observed at $\mathbf{x}_{\mathrm{A}}$ and $\mathbf{x}_{\mathrm{B}}$, along with the corresponding sources required at $\mathbf{x}$ on $\partial V^{\mathrm{a}}$ and $\partial V^{\mathrm{e}}$ for Green's function $\widehat{G}^{p,q^{\mathrm{e}}}(\mathbf{x}_{\mathrm{A}}, \mathbf{x}_{\mathrm{B}}, \omega)$ retrieval, are shown. Note that the rays in this figure represent the full responses between the source and receiver points, including primary and multiple scattering, as well as mode conversion due to inhomogeneities inside and outside the region $\partial V^{\mathrm{a}} \cup \partial V^{\mathrm{e}}$.

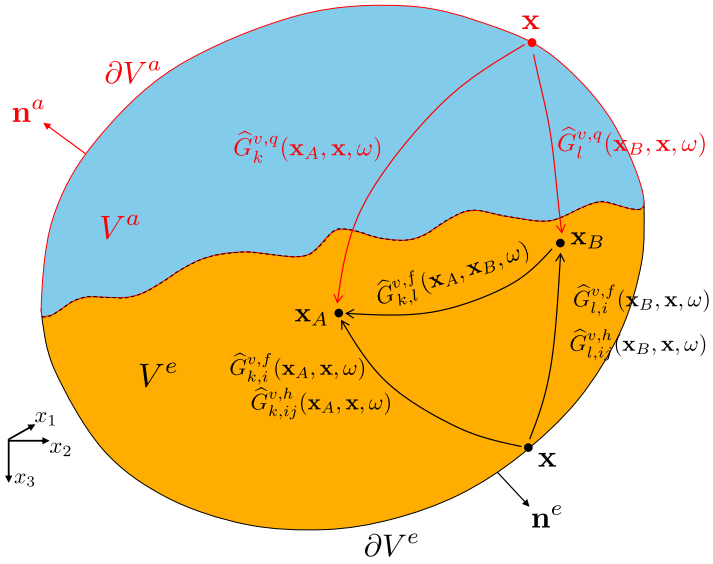


**Figure 6.** Illustration of interferometry by cross-correlation for the velocity Green's function representation when receivers are in $V^{\mathrm{e}}$. According to eq. (68), the Green's function $\widehat{G}^{v,f}_{k,l}(\mathbf{x}_{\mathrm{A}}, \mathbf{x}_{\mathrm{B}}, \omega)$ can be obtained by cross-correlating the observations at $\mathbf{x}_{\mathrm{A}}$ and $\mathbf{x}_{\mathrm{B}}$, and integrating along the source coordinate $\mathbf{x}$ at $\partial V^{\mathrm{a}}$ and $\partial V^{\mathrm{e}}$. The wavefields observed at $\mathbf{x}_{\mathrm{A}}$ and $\mathbf{x}_{\mathrm{B}}$, along with the corresponding sources required at $\mathbf{x}$ on $\partial V^{\mathrm{a}}$ and $\partial V^{\mathrm{e}}$ for velocity Green's function retrieval, are shown. Note that the rays in this figure represent the full responses between the source and receiver points, including primary and multiple scattering, as well as mode conversion due to inhomogeneities inside and outside the region $\partial V^{\mathrm{a}} \cup \partial V^{\mathrm{e}}$.

**Table 5.** Choice of sources and wavefields in $V^{\mathrm{a}}$ and $V^{\mathrm{e}}$ for states $A$ and $B$, when $\mathbf{x}_{\mathrm{A}}$ and $\mathbf{x}_{\mathrm{B}}$ are in $V^{\mathrm{e}}$, to be used in the coupled convolution-type reciprocity theorem to derive velocity Green's function expression.

| Domain | Parameter | State A | State B |
|---|---|---|---|
| in $V^{\mathrm{a}}$ | $\widehat{q}(\mathbf{x}, \omega)$ | 0 | 0 |
| | $\widehat{f}_i(\mathbf{x}, \omega)$ | 0 | 0 |
| | $\widehat{p}(\mathbf{x}, \omega)$ | $\widehat{G}^{p,f}_{,k}(\mathbf{x}, \mathbf{x}_{\mathrm{A}}, \omega)$ | $\widehat{G}^{p,f}_{,l}(\mathbf{x}, \mathbf{x}_{\mathrm{B}}, \omega)$ |
| | $\widehat{v}_i(\mathbf{x}, \omega)$ | $\frac{1}{\omega\rho^{\mathrm{a}}(\mathbf{x})}\partial_i \widehat{G}^{p,f}_{,k}(\mathbf{x}, \mathbf{x}_{\mathrm{A}}, \omega)$ | $\frac{1}{\omega\rho^{\mathrm{a}}(\mathbf{x})}\partial_i \widehat{G}^{p,f}_{,l}(\mathbf{x}, \mathbf{x}_{\mathrm{B}}, \omega)$ |
| in $V^{\mathrm{e}}$ | $\widehat{h}_{ij}(\mathbf{x}, \omega)$ | 0 | 0 |
| | $\widehat{f}_i(\mathbf{x}, \omega)$ | $\delta(\mathbf{x} - \mathbf{x}_{\mathrm{A}})\,\delta_{ik}$ | $\delta(\mathbf{x} - \mathbf{x}_{\mathrm{B}})\,\delta_{il}$ |
| | $\widehat{\tau}_{ij}(\mathbf{x}, \omega)$ | $\widehat{G}^{\tau,f}_{ij,k}(\mathbf{x}, \mathbf{x}_{\mathrm{A}}, \omega)$ | $\widehat{G}^{\tau,f}_{ij,l}(\mathbf{x}, \mathbf{x}_{\mathrm{B}}, \omega)$ |
| | $\widehat{v}_i(\mathbf{x}, \omega)$ | $\widehat{G}^{v,f}_{i,k}(\mathbf{x}, \mathbf{x}_{\mathrm{A}}, \omega)$ | $\widehat{G}^{v,f}_{i,l}(\mathbf{x}, \mathbf{x}_{\mathrm{B}}, \omega)$ |

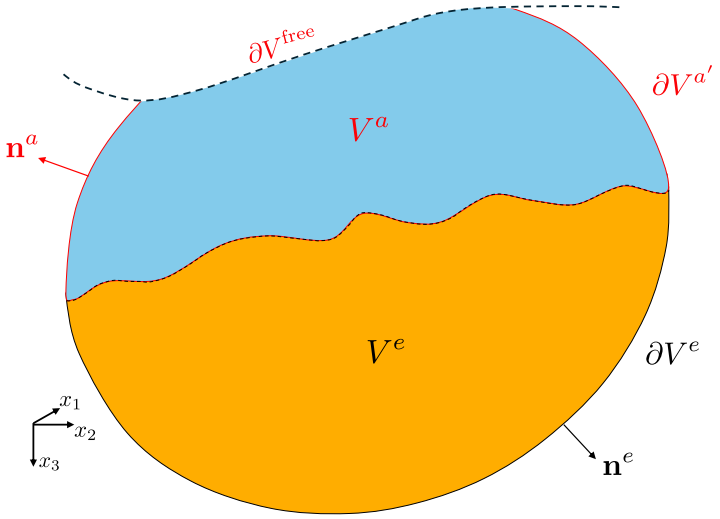


**Figure 7.** Modified configuration with a free surface $\partial V^{\text{free}}$.

relation (eq. 14) yields

$$\begin{aligned}
&\widehat{G}^{v,f*}_{l,k}(\mathbf{x}_\mathrm{B},\mathbf{x}_\mathrm{A},\omega)+\widehat{G}^{v,f}_{k,l}(\mathbf{x}_\mathrm{A},\mathbf{x}_\mathrm{B},\omega)\\
&\quad=\oint_{\partial V^\mathrm{a}}\frac{-1}{J\omega\rho^\mathrm{a}(\mathbf{x})}\left(\widehat{G}^{p,f*}_{,k}(\mathbf{x},\mathbf{x}_\mathrm{A},\omega)\partial_i\widehat{G}^{p,f}_{,l}(\mathbf{x},\mathbf{x}_\mathrm{B},\omega)-\partial_i\widehat{G}^{p,f*}_{,k}(\mathbf{x},\mathbf{x}_\mathrm{A},\omega)\widehat{G}^{p,f}_{,l}(\mathbf{x},\mathbf{x}_\mathrm{B},\omega)\right)n_i^\mathrm{a}\,\mathrm{d}^2\mathbf{x}\\
&\quad-\oint_{\partial V^\mathrm{e}}\left(\widehat{G}^{v,f*}_{i,k}(\mathbf{x},\mathbf{x}_\mathrm{A},\omega)\widehat{G}^{\tau,f}_{ij,l}(\mathbf{x},\mathbf{x}_\mathrm{B},\omega)+\widehat{G}^{\tau,f*}_{ij,k}(\mathbf{x},\mathbf{x}_\mathrm{A},\omega)\widehat{G}^{v,f}_{i,l}(\mathbf{x},\mathbf{x}_\mathrm{B},\omega)\right)n_j^\mathrm{e}\,\mathrm{d}^2\mathbf{x}.
\end{aligned}\tag{67}$$

Applying source–receiver reciprocity of eqs (21), (28) and (29) yields

$$\begin{aligned}
&2\,\Re\left\{\widehat{G}^{v,f}_{k,l}(\mathbf{x}_\mathrm{A},\mathbf{x}_\mathrm{B},\omega)\right\}\\
&=\oint_{\partial V^\mathrm{a}}\frac{-1}{J\omega\rho^\mathrm{a}(\mathbf{x})}\left(\widehat{G}^{v,q*}_{k}(\mathbf{x}_\mathrm{A},\mathbf{x},\omega)\partial_i\widehat{G}^{v,q}_{l}(\mathbf{x}_\mathrm{B},\mathbf{x},\omega)-\partial_i\widehat{G}^{v,q*}_{k}(\mathbf{x}_\mathrm{A},\mathbf{x},\omega)\widehat{G}^{v,q}_{l}(\mathbf{x}_\mathrm{B},\mathbf{x},\omega)\right)n_i^\mathrm{a}\,\mathrm{d}^2\mathbf{x}\\
&-\oint_{\partial V^\mathrm{e}}\left(\widehat{G}^{v,f*}_{k,i}(\mathbf{x}_\mathrm{A},\mathbf{x},\omega)\widehat{G}^{v,h}_{l,ij}(\mathbf{x}_\mathrm{B},\mathbf{x},\omega)+\widehat{G}^{v,h*}_{k,ij}(\mathbf{x}_\mathrm{A},\mathbf{x},\omega)\widehat{G}^{v,f}_{l,i}(\mathbf{x}_\mathrm{B},\mathbf{x},\omega)\right)n_j^\mathrm{e}\,\mathrm{d}^2\mathbf{x}.
\end{aligned}\tag{68}$$

Fig. 6 illustrates the Green's functions of the above equation observed at $\mathbf{x}_\mathrm{A}$ and $\mathbf{x}_\mathrm{B}$, along with the corresponding sources required at $\mathbf{x}$ on $\partial V^\mathrm{a}$ and $\partial V^\mathrm{e}$ to obtain the Green's function $\widehat{G}^{v,f}_{k,l}(\mathbf{x}_\mathrm{A},\mathbf{x}_\mathrm{B},\omega)$. The above expression provides an exact representation of the elastodynamic Green's function in a coupled system. However, similar to the case of the pressure Green's function, it is not particularly useful in its current form due to the superposition of two correlation products under both integrals, as well as the need for different source types on the boundary. To address this, we again approximate the acoustic and elastic boundary integrals by adopting a similar approach and assumptions as in the simplification of the pressure Green's function in Section 3.2.1. Assuming homogeneous material properties at and outside of boundaries $\partial V^\mathrm{a}$ and $\partial V^\mathrm{e}$ leads to the following result:

$$\begin{aligned}
\Re\left\{\widehat{G}^{v,f}_{k,l}(\mathbf{x}_\mathrm{A},\mathbf{x}_\mathrm{B},\omega)\right\}\approx&\frac{1}{\rho^\mathrm{a}c^\mathrm{a}}\oint_{\partial V^\mathrm{a}}\widehat{G}^{v,q*}_{k}(\mathbf{x}_\mathrm{A},\mathbf{x},\omega)\widehat{G}^{v,q}_{l}(\mathbf{x}_\mathrm{B},\mathbf{x},\omega)\,\mathrm{d}^2\mathbf{x}\\
&+\frac{1}{\rho^\mathrm{e}c^K}\oint_{\partial V^\mathrm{e}}\widehat{G}^{v,\phi*}_{k,K}(\mathbf{x}_\mathrm{A},\mathbf{x},\omega)\,\widehat{G}^{v,\phi}_{l,K}(\mathbf{x}_\mathrm{B},\mathbf{x},\omega)\,\mathrm{d}^2\mathbf{x}.
\end{aligned}\tag{69}$$

The above approximation is again highly accurate when $\partial V^\mathrm{a}$ and $\partial V^\mathrm{e}$ are portions of a sphere with a sufficiently large radius, such that all rays are normal to $\partial V^\mathrm{a}$ and $\partial V^\mathrm{e}$. In other cases, the approximation primarily introduces amplitude errors but correctly retrieves the phases of all arrivals. However, it may also lead to artifacts due to incomplete destructive interference of events, which would otherwise be fully cancelled when using the exact form in eq. (68).

### 3.4 Configuration with a free surface

We consider a modified configuration (Fig. 7) in which the closed surface is defined as $\partial V=\partial V^{a'}\cup\partial V^{\text{free}}\cup\partial V^e$. Here, $\partial V^{\text{free}}$ represents a portion of the Earth's free surface, $\partial V^{a'}$ is an arbitrarily shaped surface enclosing part of the closed surface within the acoustic medium, and $\partial V^e$ bounds the elastic solid part of the closed surface (see Fig. 7). $\partial V^{a'}$ and $\partial V^e$ do not necessarily coincide with a physical boundary. The observation points $\mathbf{x}_\mathrm{A}$ and $\mathbf{x}_\mathrm{B}$ are located within the volume enclosed by $\partial V^{a'}\cup\partial V^{\text{free}}\cup\partial V^e$. For this configuration, the results derived in the

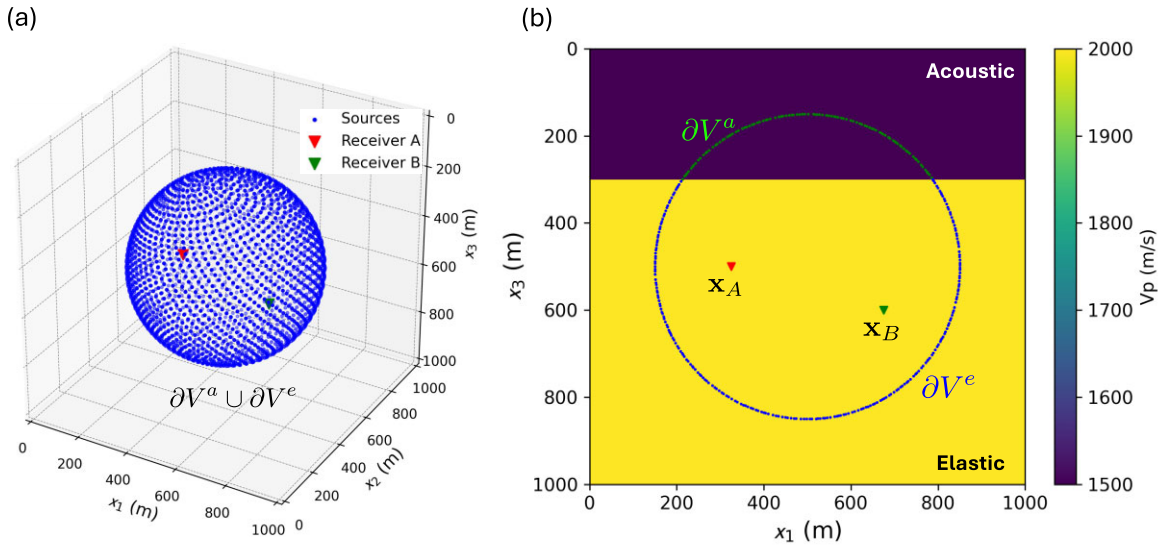


**Figure 8.** (a) Uniform source distribution on a sphere of radius 0.35 km enclosing the receivers $\mathbf{x}_A$ and $\mathbf{x}_B$, to model the retrieved Green's function (RHS of eq. 68 in time domain for $k, l = 3$) convolved with the source wavelet. (b) $x_1 - x_3$ cross-section of source and $c_P$ model through $x_2 = 0.5$ km.

previous sections for the pressure and velocity Green's functions can be directly applied. Because the acoustic pressure $p(\mathbf{x}, \omega)$ vanishes on $\partial V^{\text{free}}$, the integral $\oint_{\partial V^a}$ appearing in equations above need only only be evaluated over $\partial V^{a'}$. Consequently, Green's functions $\widehat{G}^{p,q}(\mathbf{x}_A, \mathbf{x}_B, \omega)$ and $\widehat{G}^{v,f}_{k,l}(\mathbf{x}_A, \mathbf{x}_B, \omega)$ can be obtained by cross-correlating and integrating the responses of sources located solely on $\partial V^{a'}$ and $\partial V^e$; no sources are needed on the free-surface boundary $\partial V^{\text{free}}$.

### 3.5 Numerical example

We illustrate the validity of eq. (68) using a 3-D numerical example. The model consists of a coupled acoustic–elastic domain measuring 1.0 km × 1.0 km × 1.0 km ($x_1 \times x_2 \times x_3$) discretized with uniform grid spacing of 0.01 km × 0.01 km × 0.01 km ($\mathrm{d}x_1 \times \mathrm{d}x_2 \times \mathrm{d}x_3$). The acoustic region occupies the upper 0.30 km of the model and is characterized by $c_P = 1500$ m s$^{-1}$ and $\rho = 1000$ kg m$^{-3}$. In the elastic region, we set $c_P = 2000$ m s$^{-1}$, $c_S = 1100$ m s$^{-1}$, and $\rho = 2250$ kg m$^{-3}$. To compute the retrieved Green's function, we uniformly distribute 20,000 sources over a spherical surface of 0.35 km radius centred at [0.50, 0.50, 0.50] km using the Fibonacci sphere algorithm (Keinert *et al.* 2015). The spherical source distribution encloses the receiver locations $\mathbf{x}_A = [0.325, 0.50, 0.50]$ km and $\mathbf{x}_B = [0.675, 0.50, 0.60]$ km. Fig. 8 shows the spherical source distribution, the receiver locations $\mathbf{x}_A$ and $\mathbf{x}_B$, and a cross-section of the $x_1$-$x_3$ plane through the centre of the $c_P$ model. All external model boundaries are treated as absorbing. To compute the Green's functions appearing on the right-hand integrand in eq. (68), we use the source–receiver reciprocity of eqs (21), (28) and (29). We use a Gaussian source wavelet with a narrow half-width of 12 ms to simulate the Green's functions in eq. (28). To suppress numerical noise prior to comparison, both sides of eq. (68) are convolved with a 30 Hz central frequency Ricker wavelet.

Fig. 9(a) shows the time-domain representation of individual traces of the integrand on the right of eq. (68) for the case $k, l = 3$ after convolution with the 30 Hz Ricker wavelet. Each trace corresponds to a fixed source position $\mathbf{x}$ on $\partial V^{\text{a}} \cup \partial V^{\text{e}}$, ordered from the top to the bottom of the enclosing sphere (see Fig. 8a). Fig. 9(b) shows the summation of all traces, representing the retrieved velocity Green's function $G^{v,f}_{3,3}(\mathbf{x}_A, \mathbf{x}_B)$ convolved with the wavelet. This result accurately matches the overlain time-domain representation of the left-hand side of eq. (68), that is, $G^{v,f}_{3,3}(\mathbf{x}_A, \mathbf{x}_B, -t) + G^{v,f}_{3,3}(\mathbf{x}_A, \mathbf{x}_B, t)$, also convolved with the same 30 Hz Ricker wavelet. The main contributions to the retrieved velocity Green's function come from the Fresnel zones around the stationary points of the integrand. The causal arrivals are associated with stationary-point sources located to the right of $\mathbf{x}_B$, while the anticausal arrivals originate from stationary-point sources located to the left of $\mathbf{x}_A$. Figs 9(c) and (d) respectively show zoomed-in views of the causal direct and reflected events from the acoustic–elastic coupled boundary, demonstrating close agreement between the retrieved and true Green's functions.

## 4 UNCORRELATED AMBIENT SOURCES

### 4.1 Green's function through uncorrelated ambient sources

The previous sections assumed that the sources on the boundaries $\partial V^{\text{a}}$ and $\partial V^{\text{e}}$ are impulsive point sources. However, many ocean-bottom SI studies (de Ridder & Dellinger 2011; Girard *et al.* 2023, 2024) rely on ambient sources. Therefore, in this section, we consider mutually

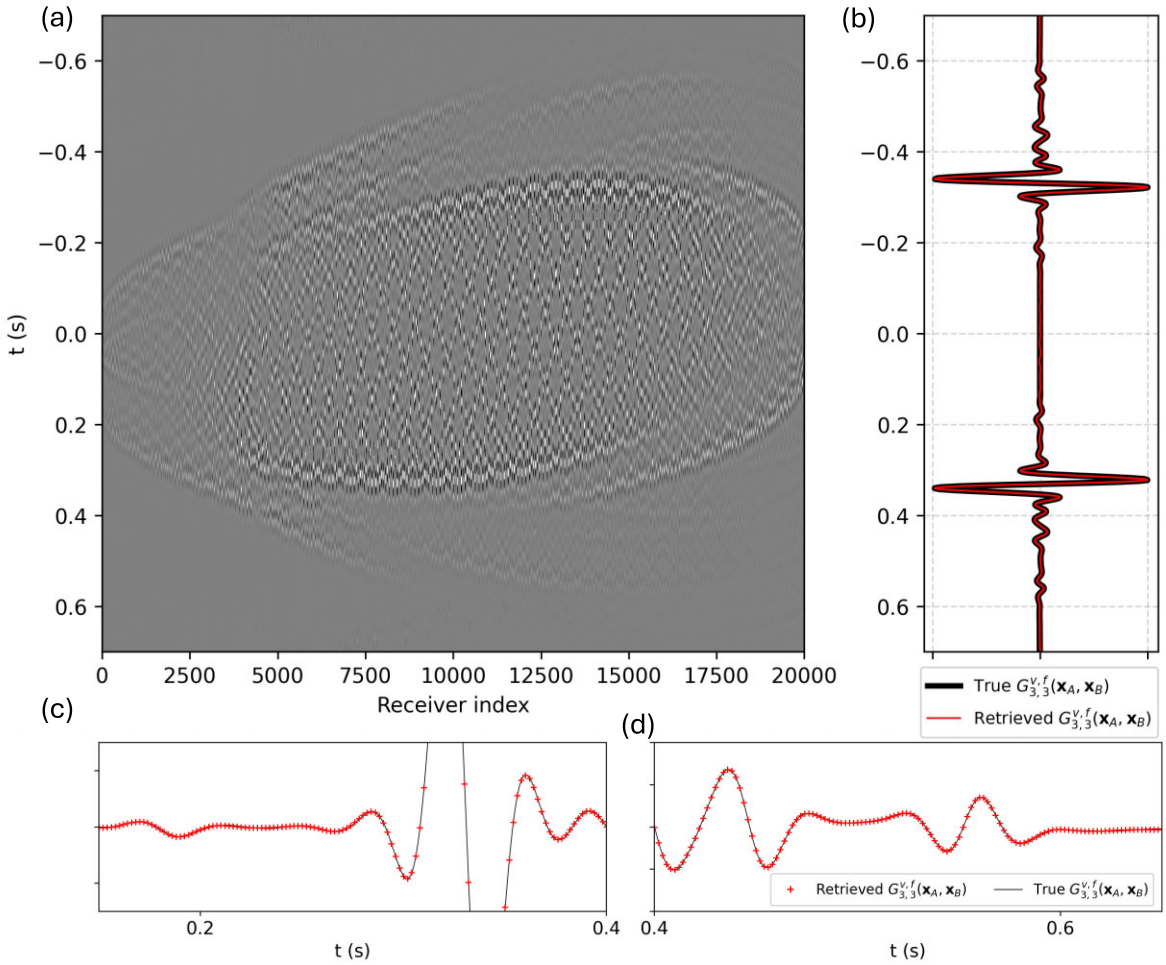


**Figure 9.** (a) Time-domain representation of individual traces of the right-hand side integrand in eq. (68) for $k, l = 3$. (b) Retrieved Green's function (red), that is, the sum of all traces shown in panel (a), overlain on the true Green's function (black). (c) Zoomed-in view of the causal direct arrival events in (b). The solid black line represents the true Green's function $G^{v,f}_{3,3}(\mathbf{x}_\mathrm{A}, \mathbf{x}_\mathrm{B})$, and the red plus signs (+) denote the retrieved Green's function. (d) Zoomed-in view of the causal reflected events in panel (b) from the coupled acoustic–elastic boundary.

uncorrelated ambient sources (Weaver & Lobkis 2001; Snieder 2004; Wapenaar 2004; Shapiro *et al.* 2005; Wapenaar & Fokkema 2006) acting on these boundaries.

We assume that ambient sources are acting on a closed surface $\partial V^\mathrm{a} \cup \partial V^\mathrm{e}$ (see Fig. 1) with volume injection rate sources on $\partial V^\mathrm{a}$ and *P*- and *S*-wave source type on $\partial V^\mathrm{e}$. When all ambient sources act simultaneously, the observed particle velocity wavefield $\widehat{v}^{obs}_k$ at $\mathbf{x}_\mathrm{A}$ and $\mathbf{x}_\mathrm{B}$ can be expressed as

$$\widehat{v}^{obs}_k(\mathbf{x}_\mathrm{A}, \omega) = \int_{\partial V^\mathrm{a}} \widehat{G}^{v,q}_k(\mathbf{x}_\mathrm{A}, \mathbf{x}^\mathrm{a}, \omega)\widehat{N}^q(\mathbf{x}^\mathrm{a}, \omega)\, \mathrm{d}^2\mathbf{x}^\mathrm{a} + \int_{\partial V^\mathrm{e}} \widehat{G}^{v,\phi}_{k,K}(\mathbf{x}_\mathrm{A}, \mathbf{x}^\mathrm{e}, \omega)\widehat{N}_K(\mathbf{x}^\mathrm{e}, \omega)\, \mathrm{d}^2\mathbf{x}^\mathrm{e} \tag{70}$$

and

$$\widehat{v}^{obs}_l(\mathbf{x}_\mathrm{B}, \omega) = \int_{\partial V^\mathrm{a}} \widehat{G}^{v,q}_l(\mathbf{x}_\mathrm{B}, \mathbf{x}^{a'}, \omega)\widehat{N}^q(\mathbf{x}^{a'}, \omega)\, \mathrm{d}^2\mathbf{x}^{a'} + \int_{\partial V^\mathrm{e}} \widehat{G}^{v,\phi}_{l,L}(\mathbf{x}_\mathrm{B}, \mathbf{x}^{e'}, \omega)\widehat{N}_L(\mathbf{x}^{e'}, \omega)\, \mathrm{d}^2\mathbf{x}^{e'}, \tag{71}$$

where $\widehat{N}^q(\mathbf{x}^a, \omega)$ and $\widehat{N}^q(\mathbf{x}^{a'}, \omega)$ are the volume injection rate-type ambient signal at the boundary $\partial V^\mathrm{a}$ with $\mathbf{x}^a$ and $\mathbf{x}^{a'}$ as acoustic boundary integration variable. $\widehat{N}_K(\mathbf{x}^e, \omega)$, $\widehat{N}_L(\mathbf{x}^{e'}, \omega)$ are the ambient signal at the boundary $\partial V^\mathrm{e}$ with $\mathbf{x}^e$ and $\mathbf{x}^{e'}$ as elastic boundary integration variable. Here, $K, L = 0$ correspond to a *P*-wave source and $K, L = 1, 2, 3$ for a *S*-wave source with different polarizations,.

The continuous cross-correlation functions (CCFs), denoted as $\widehat{\mathcal{C}}^{v,v}_{k,l}$, of the ambient wavefield recordings $\widehat{v}^{obs}_k(\mathbf{x}_\mathrm{A}, \omega)$ and $\widehat{v}^{obs}_l(\mathbf{x}_\mathrm{B}, \omega)$ can be written as

$$\widehat{\mathcal{C}}^{v,v}_{k,l}(\mathbf{x}_\mathrm{A}, \mathbf{x}_\mathrm{B}, \omega) = \widehat{v}^{obs*}_k(\mathbf{x}_\mathrm{A}, \omega)\widehat{v}^{obs}_l(\mathbf{x}_\mathrm{B}, \omega). \tag{72}$$

Here, the notation $\widehat{\mathcal{C}}^{v,v}_{k,l}$ specifies the physical quantities being cross-correlated in the superscripts and their components in the subscripts. Substituting eqs (70) and (71) into above yields

$$\begin{aligned}\widehat{\mathcal{C}}^{v,v}_{k,l}(\mathbf{x}_\mathrm{A},\mathbf{x}_B,\omega) = &\int_{\partial V^a}\int_{\partial V^a} \widehat{G}^{v,q*}_{k}(\mathbf{x}_\mathrm{A},\mathbf{x}^a,\omega)\,\widehat{G}^{v,q}_{l}(\mathbf{x}_B,\mathbf{x}^{a\prime},\omega)\,\widehat{N}^{q*}(\mathbf{x}^a,\omega)\,\widehat{N}^{q}(\mathbf{x}^{a\prime},\omega)\,\mathrm{d}^2\mathbf{x}^a\,\mathrm{d}^2\mathbf{x}^{a\prime}\\ &+\int_{\partial V^a}\int_{\partial V^e} \widehat{G}^{v,q*}_{k}(\mathbf{x}_\mathrm{A},\mathbf{x}^a,\omega)\,\widehat{G}^{v,\phi}_{l,L}(\mathbf{x}_B,\mathbf{x}^{e\prime},\omega)\,\widehat{N}^{q*}(\mathbf{x}^a,\omega)\,\widehat{N}_{L}(\mathbf{x}^{e\prime},\omega)\,\mathrm{d}^2\mathbf{x}^a\,\mathrm{d}^2\mathbf{x}^{e\prime}\\ &+\int_{\partial V^e}\int_{\partial V^a} \widehat{G}^{v,\phi*}_{k,K}(\mathbf{x}_\mathrm{A},\mathbf{x}^e,\omega)\,\widehat{G}^{v,q}_{l}(\mathbf{x}_B,\mathbf{x}^{a\prime},\omega)\,\widehat{N}^{*}_{K}(\mathbf{x}^e,\omega)\,\widehat{N}^{q}(\mathbf{x}^{a\prime},\omega)\,\mathrm{d}^2\mathbf{x}^e\,\mathrm{d}^2\mathbf{x}^{a\prime}\\ &+\int_{\partial V^e}\int_{\partial V^e} \widehat{G}^{v,\phi}_{k,K*}(\mathbf{x}_\mathrm{A},\mathbf{x}^e,\omega)\,\widehat{G}^{v,\phi}_{l,L}(\mathbf{x}_B,\mathbf{x}^{e\prime},\omega)\,\widehat{N}^{*}_{K}(\mathbf{x}^e,\omega)\,\widehat{N}_{L}(\mathbf{x}^{e\prime},\omega)\,\mathrm{d}^2\mathbf{x}^e\,\mathrm{d}^2\mathbf{x}^{e\prime}.\end{aligned} \tag{73}$$

We assume that two ambient sources are mutually uncorrelated so that they obey

$$\langle \widehat{N}^{q*}(\mathbf{x}^a,\omega)\,\widehat{N}_{L}(\mathbf{x}^{e\prime},\omega)\rangle = \langle \widehat{N}^{*}_{K}(\mathbf{x}^e,\omega)\,\widehat{N}^{q}(\mathbf{x}^{a\prime},\omega)\rangle = 0. \tag{74}$$

However, same ambient-source types result in

$$\langle \widehat{N}^{q*}(\mathbf{x}^a,\omega)\,\widehat{N}^{q}(\mathbf{x}^{a\prime},\omega)\rangle = \frac{1}{\rho^\mathrm{a}c^\mathrm{a}}\delta(\mathbf{x}^a-\mathbf{x}^{a\prime})\widehat{S}(\omega) \tag{75}$$

and

$$\langle \widehat{N}^{*}_{K}(\mathbf{x}^e,\omega)\,\widehat{N}_{L}(\mathbf{x}^{e\prime},\omega)\rangle = \frac{1}{\rho^\mathrm{e}c^K}\delta_{KL}\,\delta(\mathbf{x}^e-\mathbf{x}^{e\prime})\widehat{S}(\omega), \tag{76}$$

where $\langle\cdot\rangle$ denotes an ensemble average; $\delta(\mathbf{x})$ is a 2-D spatial delta function; and $\widehat{S}(\omega)$ is the ambient source power spectrum. All sources are assumed to have the same power spectra for all $\mathbf{x}$ but different power normalization factors, $1/(\rho^\mathrm{a}c^\mathrm{a})$ for $\mathbf{x}$ at $\partial V^\mathrm{a}$ and $1/(\rho^\mathrm{e}c^K)$ for $\mathbf{x}$ at $\partial V^\mathrm{e}$, respectively. Taking the ensemble average of eq. (73), accounting for eqs (74)–(76) and keeping a single integration variable $\mathbf{x}\in\{\mathbf{x}^\mathrm{a},\mathbf{x}^\mathrm{e}\}$ for both the boundaries $\partial V^\mathrm{a}$ and $\partial V^\mathrm{e}$, eq. (73) yields the ensemble cross-correlation

$$\begin{aligned}\langle\widehat{\mathcal{C}}^{v,v}_{k,l}(\mathbf{x}_\mathrm{A},\mathbf{x}_\mathrm{B},\omega)\rangle = &\frac{1}{\rho^\mathrm{a}c^\mathrm{a}}\int_{\partial V^\mathrm{a}} \widehat{G}^{v,q*}_{k}(\mathbf{x}_\mathrm{A},\mathbf{x},\omega)\,\widehat{G}^{v,q}_{l}(\mathbf{x}_\mathrm{B},\mathbf{x},\omega)\,\widehat{S}(\omega)\,\mathrm{d}^2\mathbf{x}\\ &+\frac{1}{\rho^\mathrm{e}c^K}\int_{\partial V^\mathrm{e}} \widehat{G}^{v,\phi*}_{k,K}(\mathbf{x}_\mathrm{A},\mathbf{x},\omega)\,\widehat{G}^{v,\phi}_{l,K}(\mathbf{x}_\mathrm{B},\mathbf{x},\omega)\,\widehat{S}(\omega)\,\mathrm{d}^2\mathbf{x}.\end{aligned} \tag{77}$$

Combining this with eq. (69) (considering the case when $\mathbf{x}_\mathrm{A}$ and $\mathbf{x}_\mathrm{B}$ lie within $V^\mathrm{e}$) obtains

$$\Re\{\widehat{G}^{v,f}_{k,l}(\mathbf{x}_\mathrm{A},\mathbf{x}_\mathrm{B},\omega)\}S(\omega) \approx \langle\widehat{\mathcal{C}}^{v,v}_{k,l}(\mathbf{x}_\mathrm{A},\mathbf{x}_\mathrm{B},\omega)\rangle. \tag{78}$$

This relation suggests that the velocity CCFs due to uncorrelated ambient sources can be approximated by the velocity Green's function, $\widehat{G}^{v,f}_{k,l}$, multiplied with the power spectra of the ambient sources, under the following conditions: the medium at and outside $\partial V^\mathrm{a}$ and $\partial V^\mathrm{e}$ is homogeneous; uniform volume injection rate sources with strength $\sqrt{1/(\rho^\mathrm{a}c^\mathrm{a})}$ are present at the boundary $\partial V^\mathrm{a}$; and uniform *P*- and *S*-wave ambient sources with strength $\sqrt{1/(\rho^\mathrm{e}c^K)}$ are present at the boundary $\partial V^\mathrm{e}$.

For the case where the CCF pertains to pressure, a similar convergence to the pressure Green's function can be derived as

$$\Re\{\widehat{G}^{p,q}(\mathbf{x}_\mathrm{A},\mathbf{x}_\mathrm{B},\omega)\}S(\omega) \approx \langle\widehat{\mathcal{C}}^{p,p}(\mathbf{x}_\mathrm{A},\mathbf{x}_\mathrm{B},\omega)\rangle. \tag{79}$$

Although eqs (78) and (79) demonstrate the recovery of interstation Green's functions through ambient cross-correlations, their applicability to practical marine SI problems is limited due to heterogeneous source distribution and the unavailability of sources of different types and at depths.

### 4.2 Modelling low-frequency ambient cross-correlation functions for ocean-bottom sensors

In practical marine scenarios, the conditions required for Green's function retrieval through CCFs are rarely satisfied primarily due to the absence of an ideal ambient source distribution. Ambient sources in oceanic regions predominantly originate from pressure fluctuations at the Earth's surface that are driven by interactions between wind-generated ocean storms and ocean-wave breaking, which induce pressure variations at the seafloor capable of generating seismic waves in the Earth. It is well known that these sources are often spatially non-uniform. Notably, there are no microseism sources within the solid Earth's volume itself. As a result, ambient sources caused by ocean-wave interactions at the surface, known as secondary microseisms, are typically modelled as non-zero pressure source distributions at the ocean surface and sources arising from the interaction of long-wavelength ocean waves with local bathymetry, referred to as primary microseisms, are approximated as point force sources acting at the local bathymetry (Hasselmann 1963; Ardhuin & Herbers 2013; Ardhuin *et al.* 2015; Nakata *et al.* 2019).

We first derive the CCF expression for ambient sources modelled as point force sources acting on the ocean bottom. However, as mentioned above, these sources also can be volume injection rate sources acting at the ocean surface. Below, we also develop expressions for volume injection rate-type ambient sources. We refer this approach herein as cross-correlation modelling (CCM).

We may write the observed wavefield $\widehat{v}_k^{obs}(\mathbf{x}, \omega)$ due to ambient sources as

$$\widehat{v}_k^{obs}(\mathbf{x}, \omega) = \int_{\partial D} \widehat{G}_{k,n}^{v,f}(\mathbf{x}, \boldsymbol{\xi}, \omega)\widehat{N}_n(\boldsymbol{\xi}, \omega)\, \mathrm{d}\boldsymbol{\xi}, \tag{80}$$

where $\widehat{N}_n(\boldsymbol{\xi}, \omega)$ denotes the $n$th component of the ambient force source; and $\partial D$ is the region where these sources are present, which in this case is the ocean bottom. Substituting eq. (80) into eq. (72) for observed wavefield recorded at $\mathbf{x}_\mathrm{A}$ and $\mathbf{x}_\mathrm{B}$ from ambient sources at $\boldsymbol{\xi}_1$ and $\boldsymbol{\xi}_2$, respectively, results in the CCF expression

$$\widehat{\mathcal{C}}_{k,l}^{v,v}(\mathbf{x}_\mathrm{A}, \mathbf{x}_\mathrm{B}, \omega) = \iint_{\partial D} \widehat{G}_{k,n}^{v,f*}(\mathbf{x}_\mathrm{A}, \boldsymbol{\xi}_1, \omega)\, \widehat{G}_{l,m}^{v,f}(\mathbf{x}_\mathrm{B}, \boldsymbol{\xi}_2, \omega)\, \widehat{N}_n^*(\boldsymbol{\xi}_1, \omega)\, \widehat{N}_m(\boldsymbol{\xi}_2, \omega)\, \mathrm{d}\boldsymbol{\xi}_1\, \mathrm{d}\boldsymbol{\xi}_2. \tag{81}$$

Usually, large numbers of windowed cross-correlations of continuous ambient wavefield recordings are stacked to enhance coherent signals and downweight incoherent noise. We take the ensemble average of CCF and assume that the ambient force sources are uncorrelated as

$$\langle \widehat{N}_n^*(\boldsymbol{\xi}_1, \omega)\widehat{N}_m(\boldsymbol{\xi}_2, \omega)\rangle = \widehat{S}(\boldsymbol{\xi}_1, \omega)\delta_{nm}\, \delta(\boldsymbol{\xi}_1 - \boldsymbol{\xi}_2) \tag{82}$$

to simplify eq. (81) to

$$\langle \widehat{\mathcal{C}}_{k,l}^{v,v}(\mathbf{x}_\mathrm{A}, \mathbf{x}_\mathrm{B}, \omega)\rangle = \int_{\partial D} \widehat{G}_{k,n}^{v,f*}(\mathbf{x}_\mathrm{A}, \boldsymbol{\xi}, \omega)\widehat{G}_{l,n}^{v,f}(\mathbf{x}_\mathrm{B}, \boldsymbol{\xi}, \omega)\widehat{S}(\boldsymbol{\xi}, \omega)\mathrm{d}\boldsymbol{\xi}, \tag{83}$$

where $\widehat{S}(\boldsymbol{\xi}, \omega)$ denotes the power-spectral density of the ambient source (Tromp *et al.* 2010). For a narrow frequency band (e.g. 0.05–1.0 Hz), $S(\boldsymbol{\xi}, \omega)$ can be partitioned into its spatial and frequency dependencies as

$$\widehat{S}(\boldsymbol{\xi}, \omega) = S(\boldsymbol{\xi})\widehat{S}(\omega), \tag{84}$$

where the relative spatial distribution of ambient wavefield energy is defined such that $S(\boldsymbol{\xi}) = 0$ and $S(\boldsymbol{\xi}) = 1$ represent effective sources with zero and the highest energy at location $\boldsymbol{\xi}$, respectively; and $\widehat{S}(\omega)$ is the power spectrum of ambient wavefield sources. With these definitions, the CCF becomes

$$\langle \widehat{\mathcal{C}}_{k,l}^{v,v}(\mathbf{x}_\mathrm{A}, \mathbf{x}_\mathrm{B}, \omega)\rangle = \int_{\partial D} \widehat{G}_{k,n}^{v,f*}(\mathbf{x}_\mathrm{A}, \boldsymbol{\xi}, \omega)\, \widehat{G}_{l,n}^{v,f}(\mathbf{x}_\mathrm{B}, \boldsymbol{\xi}, \omega)S(\boldsymbol{\xi})\widehat{S}(\omega)\mathrm{d}\boldsymbol{\xi}, \tag{85}$$

or rearranging after using source–receiver reciprocity (eq. 28):

$$\langle \widehat{\mathcal{C}}_{k,l}^{v,v}(\mathbf{x}_\mathrm{A}, \mathbf{x}_\mathrm{B}, \omega)\rangle = \int_{\partial D} \widehat{G}_{l,n}^{v,f}(\mathbf{x}_\mathrm{B}, \boldsymbol{\xi}, \omega)\left\{\left(\widehat{G}_{n,k}^{v,f*}(\boldsymbol{\xi}, \mathbf{x}_\mathrm{A}, \omega)S(\boldsymbol{\xi})\right)\widehat{S}(\omega)\right\}\mathrm{d}\boldsymbol{\xi}. \tag{86}$$

Comparing the above with eq. (80) and setting $\mathbf{x}_B = \mathbf{x}$ allows us to interpret the above expression as an observed wavefield generated by the driving source,

$$\widehat{f}_n(\boldsymbol{\xi}, \mathbf{x}_\mathrm{A}, \omega) = \widehat{G}_{n,k}^{v,f*}(\boldsymbol{\xi}, \mathbf{x}_\mathrm{A}, \omega)S(\boldsymbol{\xi})\widehat{S}(\omega), \tag{87}$$

also known as the 'generating wavefield' (Tromp *et al.* 2010). Because complex conjugation in the frequency domain is time-reversal in time domain, the 'generating wavefield' is simply the ambient source-energy-weighted time-reversed wavefield recorded at ambient source locations $\boldsymbol{\xi}$ due to a source at the virtual shot point locations $\mathbf{x}_\mathrm{A}$ with power spectrum $S(\omega)$. In the time domain, eq. (86) can be represented as

$$\langle \mathcal{C}_{k,l}^{v,v}(\mathbf{x}_\mathrm{A}, \mathbf{x}_\mathrm{B}, t)\rangle = \int_{\partial D} G_{l,n}^{v,f}(\mathbf{x}_\mathrm{B}, \boldsymbol{\xi}, t) * \left\{\left(G_{n,k}^{v,f}(\boldsymbol{\xi}, \mathbf{x}_\mathrm{A}, -t)S(\boldsymbol{\xi})\right) * S(t)\right\}\mathrm{d}\boldsymbol{\xi}, \tag{88}$$

where $*$ denote the convolution operator; and $S(t)$ is ambient-source autocorrelation time function. Note the summation convention in the above equation, implying that the term on the right-hand side must be computed for $n = 1, 2, 3$, accounting for all the force components, to evaluate $\langle \mathcal{C}_{k,l}^{v,v}\rangle$, that is,

$$\begin{aligned}\langle \mathcal{C}_{k,l}^{v,v}(\mathbf{x}_\mathrm{A}, \mathbf{x}_\mathrm{B}, t)\rangle = &\int_{\partial D} G_{l,1}^{v,f}(\mathbf{x}_\mathrm{B}, \boldsymbol{\xi}, t) * \left\{\left(G_{1,k}^{v,f}(\boldsymbol{\xi}, \mathbf{x}_\mathrm{A}, -t)S(\boldsymbol{\xi})\right) * S(t)\right\}\mathrm{d}\boldsymbol{\xi}\\ &+ \int_{\partial D} G_{l,2}^{v,f}(\mathbf{x}_\mathrm{B}, \boldsymbol{\xi}, t) * \left\{\left(G_{2,k}^{v,f}(\boldsymbol{\xi}, \mathbf{x}_\mathrm{A}, -t)S(\boldsymbol{\xi})\right) * S(t)\right\}\mathrm{d}\boldsymbol{\xi}\\ &+ \int_{\partial D} G_{l,3}^{v,f}(\mathbf{x}_\mathrm{B}, \boldsymbol{\xi}, t) * \left\{\left(G_{3,k}^{v,f}(\boldsymbol{\xi}, \mathbf{x}_\mathrm{A}, -t)S(\boldsymbol{\xi})\right) * S(t)\right\}\mathrm{d}\boldsymbol{\xi}.\end{aligned} \tag{89}$$

For ambient-energy sources acting on ocean surface as distributed volume injection rate sources, denoted by $q$, we may write eq. (85) as

$$\langle \widehat{\mathcal{C}}_{k,l}^{v,v}(\mathbf{x}_\mathrm{A}, \mathbf{x}_\mathrm{B}, \omega)\rangle = \int_{\partial D} \widehat{G}_k^{v,q*}(\mathbf{x}_\mathrm{A}, \boldsymbol{\xi}, \omega)\widehat{G}_l^{v,q}(\mathbf{x}_\mathrm{B}, \boldsymbol{\xi}, \omega)S(\boldsymbol{\xi})\widehat{S}(\omega)\, \mathrm{d}\boldsymbol{\xi}. \tag{90}$$

Using source-reciprocity relation (eq. (21)) and arranging the above equation gives

$$\langle \widehat{\mathcal{C}}_{k,l}^{v,v}(\mathbf{x}_\mathrm{A}, \mathbf{x}_\mathrm{B}, \omega)\rangle = -\int_{\partial D} \widehat{G}_l^{v,q}(\mathbf{x}_\mathrm{B}, \boldsymbol{\xi}, \omega)\left\{\left(\widehat{G}_{,k}^{p,f*}(\boldsymbol{\xi}, \mathbf{x}_\mathrm{A}, \omega)S(\boldsymbol{\xi})\right)\widehat{S}(\omega)\right\}\mathrm{d}\boldsymbol{\xi}, \tag{91}$$

**Table 6.** Velocity model parameters for numerical example.

| Domain | *P*-wave velocity $c_P$ (m s$^{-1}$) | *S*-wave velocity $c_S$ (m s$^{-1}$) | Density $\rho$ (kg m$^{-3}$) | $c_p$ gradient (km s$^{-1}$ per km) | $c_s$ gradient (km s$^{-1}$ per km) |
|---|---|---|---|---|---|
| Water | 1500 | 0 | 1000 | – | – |
| Solid | 1800 | 600 | 2100 | 0.40 | 0.23 |

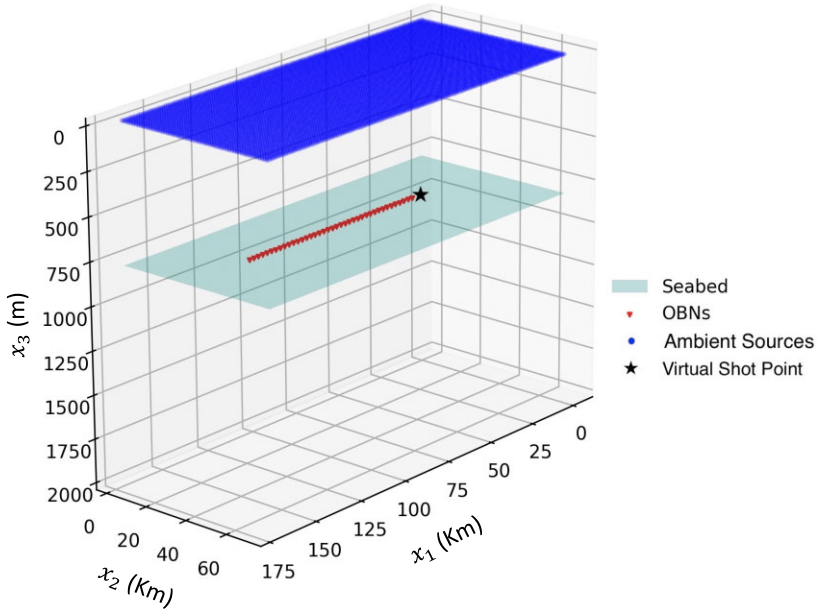


**Figure 10.** Ambient sources, OBNs and virtual shot point location for results in Figs 11 and 12.

or equivalently in the time domain

$$\langle \mathcal{C}^{v,v}_{k,l}(\mathbf{x}_A, \mathbf{x}_B, t)\rangle = -\int_{\partial D} G^{v,q}_{l}(\mathbf{x}_B, \boldsymbol{\xi}, t) * \left\{\left(G^{p,f}_{,k}(\boldsymbol{\xi}, \mathbf{x}_A, -t)S(\boldsymbol{\xi})\right) * S(t)\right\}\, \mathrm{d}\boldsymbol{\xi}. \tag{92}$$

For pressure CCFs when both receivers $\mathbf{x}_A$ and $\mathbf{x}_B$ are in water, similar time-domain equations can be written for ambient force sources

$$\langle \mathcal{C}^{p,p}(\mathbf{x}_A, \mathbf{x}_B, t)\rangle = -\int_{\partial D} G^{p,f}_{,n}(\mathbf{x}_B, \boldsymbol{\xi}, t) * \left\{\left(G^{v,q}_{n}(\boldsymbol{\xi}, \mathbf{x}_A, -t)S(\boldsymbol{\xi})\right) * S(t)\right\}\, \mathrm{d}\boldsymbol{\xi}, \tag{93}$$

and for ambient volume injection rate sources

$$\langle \mathcal{C}^{p,p}(\mathbf{x}_A, \mathbf{x}_B, t)\rangle = \int_{\partial D} G^{p,q}(\mathbf{x}_B, \boldsymbol{\xi}, t) * \{(G^{p,q}(\boldsymbol{\xi}, \mathbf{x}_A, -t)S(\boldsymbol{\xi})) * S(t)\}\, \mathrm{d}\boldsymbol{\xi}. \tag{94}$$

Eqs (88) and (92)–(94) enable the forward modelling of all (velocity and pressure) CCFs for dense OBN arrays for different ambient source types, locations and configurations.

### *4.2.1 Numerical example*

We simulate the low-frequency vertical-velocity and pressure component cross-correlation wavefields, $\langle \mathcal{C}^{v,v}_{3,3}\rangle$ and $\langle \mathcal{C}^{p,p}\rangle$, respectively, recorded on OBNs due to ambient sources acting on the ocean surface, using their corresponding CCM modelling equations (eqs 92 and 94, respectively). A detailed workflow for implementing the CCM modelling equations (eqs 88 and 92–94) in the time domain is described in Pandey *et al.* (2025). The synthetic ocean model is 176 km × 76 km × 14.6 km ($x_1 \times x_2 \times x_3$) with a regular grid spacing of 0.4 km × 0.4 km × 0.2 km ($\mathrm{d}x_1 \times \mathrm{d}x_2 \times \mathrm{d}x_3$). We assume a flat seafloor with 0.8 km water depth and 1-D $c_P(x_3)$ and $c_S(x_3)$ velocity profiles beneath the ocean bottom. Table 6 presents the model properties where the $c_P$, $c_S$ and $\rho$ in the solid medium are defined at the ocean bottom and increase with depth according to the listed gradients. The ambient source-time autocorrelation function $S(t)$ is a zero-phase Ricker wavelet with a 0.35 Hz central frequency. The time step for the simulation is 3.5 ms, with a 170 s total duration. With these parameters, the computational domain resolves a maximum frequency of 1.2 Hz. Fig. 10 shows the geometry of ambient sources, OBNs and the virtual shot point location. The ambient sources are uniformly distributed at each grid point across the ocean surface as volume injection rate sources. For velocity-velocity cross-correlations, $\langle \mathcal{C}^{v,v}_{3,3}(\mathbf{x}_A, \mathbf{x}_B, t)\rangle$, the OBNs located at $\mathbf{x}_A$ and $\mathbf{x}_B$ in eq. (92) are positioned 10 m below the seafloor, placing them within the elastic medium.

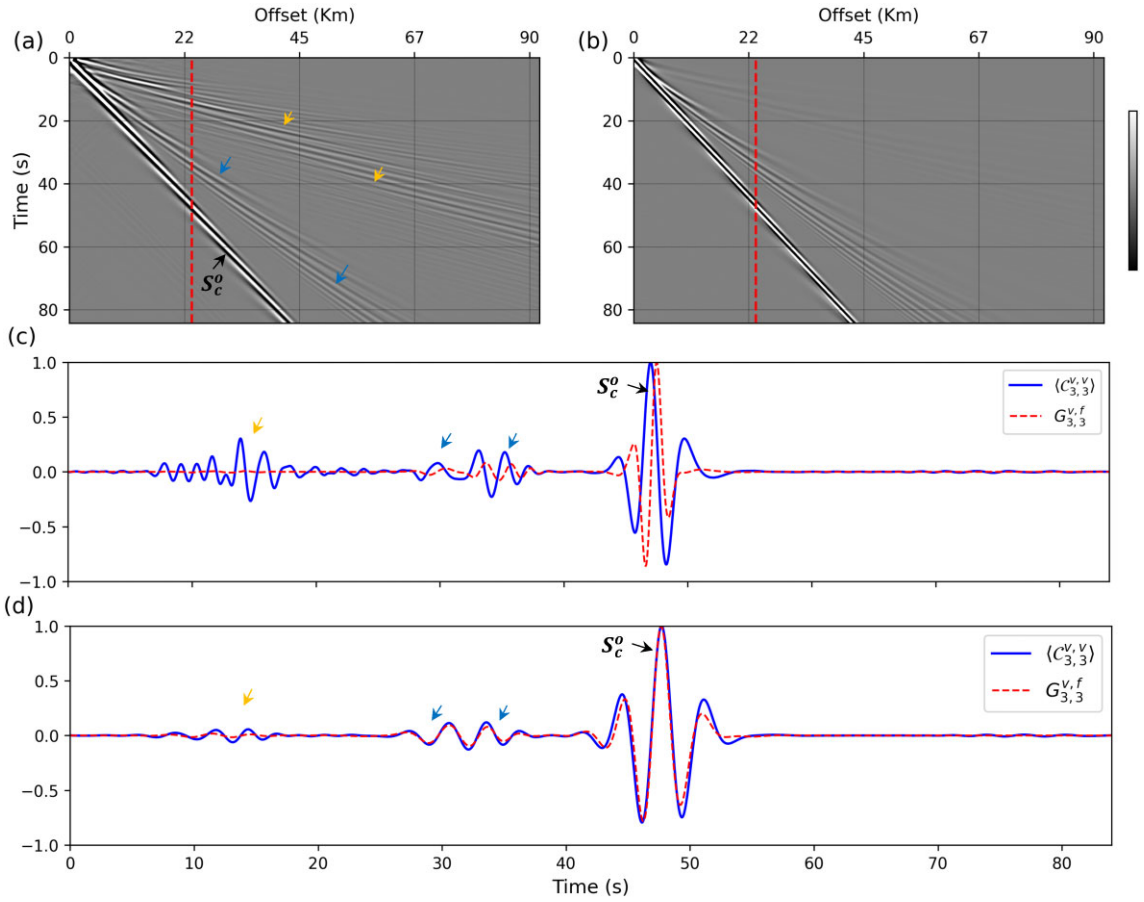


**Figure 11.** Vertical-component velocity: (a) VSG $\langle \mathcal{C}_{3,3}^{v,v} \rangle$ and (b) Green's function, $G_{3,3}^{v,f}$, for the model shown in Fig. 10. The relative amplitudes between shot gathers are not preserved. (c) Normalized traces from the location indicated by the red lines in panels (a) and (b). (d) Traces from panel (c), low-pass filtered to 0.35 Hz with $\langle \mathcal{C}_{3,3}^{v,v} \rangle$ uniformly phase-shifted by $-\pi/2$.

In contrast, for pressure-pressure cross-correlations, $\langle \mathcal{C}^{p,p}(\mathbf{x}_\mathrm{A}, \mathbf{x}_\mathrm{B}, t) \rangle$, the OBNs at $\mathbf{x}_\mathrm{A}$ and $\mathbf{x}_\mathrm{B}$ in eq. (94) are positioned 10 m above the seafloor, within the acoustic medium. In both cases, the OBNs are aligned along the $x_1$-axis. This placement ensures numerical stability in the forward modelling by avoiding coincident receiver locations with the fluid–solid boundary where coupled-interface boundary conditions are enforced. Moreover, the 10 m offset is negligible relative to the model dimensions and the dominant wavelength of the low-frequency (0.35 Hz) source wavelet used in the simulations. The virtual shot point, indicated by a star, is located at $[x_1, x_2, x_3]_\mathrm{A} = [48.0, 38.0, 0.81]$ km for $\langle \mathcal{C}_{3,3}^{v,v} \rangle$ and at $[x_1, x_2, x_3]_\mathrm{A} = [48.0, 38.0, 0.79]$ km for $\langle \mathcal{C}^{p,p} \rangle$. We use a free-surface top boundary with all other sides modelled as absorbing boundaries. We simulate forward wave propagation using SPECFEM3D Cartesian 4.1.0 (Komatitsch & Tromp 2002a, b; Komatitsch *et al.* 2023) published under the GPL3 license. The open-source software implements the 3-D spectral element method (Komatitsch *et al.* 2000) for wave propagation modelling.

Fig. 11(a) presents the causal part of the simulated $\langle \mathcal{C}_{3,3}^{v,v} \rangle$ VSG. Two distinct wave modes are evident: (1) the fundamental Scholte $S_c^0$ wave mode (black arrow) along with higher-order overtones (blue arrows); and (2) guided *P* waves (yellow arrows). These wave modes are consistent with field data VSG observations from the Gulf of Mexico, as reported in Girard *et al.* (2023, 2024). The $S_c^0$ wave mode exhibits significantly higher energy compared to its higher-order modes and the guided *P* waves.

Fig. 11(b) depicts the causal part of the vertical-component velocity Green's function, $G_{3,3}^{v,f}$, computed by injecting a vertical point force source at the virtual shot point location. In this case, the guided *P* waves are notably weaker than the $S_\mathrm{c}$ waves, and its higher-order modes are absent. Furthermore, the fundamental and higher-order Scholte wave modes display a broader frequency bandwidth in comparison to those observed in $\langle \mathcal{C}_{3,3}^{v,v} \rangle$.

Fig. 11(c) provides a trace comparison at the location marked by the red line at an offset of 24 km in Figs 11(a) and (b). The amplitudes of both traces are normalized to unity. The comparison shows a phase discrepancy, as the main peaks exhibit misalignment between the Green's function and the $\langle \mathcal{C}_{3,3}^{v,v} \rangle$ trace. Fig. 11(d) shows the traces after low-pass filtering to 0.35 Hz, with $\langle \mathcal{C}_{3,3}^{v,v} \rangle$ uniformly phase-shifted by $-\pi/2$. Following this phase adjustment, the phases of the main peaks are better aligned.

Fig. 12(a) shows the causal part of the pressure VSG $\langle \mathcal{C}^{p,p} \rangle$. In this figure, the $S_\mathrm{c}^0$ wave and its higher-order overtones (blue arrows) are weakly visible, while the guided *P* waves appear strong. Again, this observation is consistent with field-data $\langle \mathcal{C}^{p,p} \rangle$ VSG examples from the Thunderhorse field OBN array in the Gulf of Mexico, where the ocean bottom, as seen by low-frequency $S_\mathrm{c}^0$ waves, is soft with average

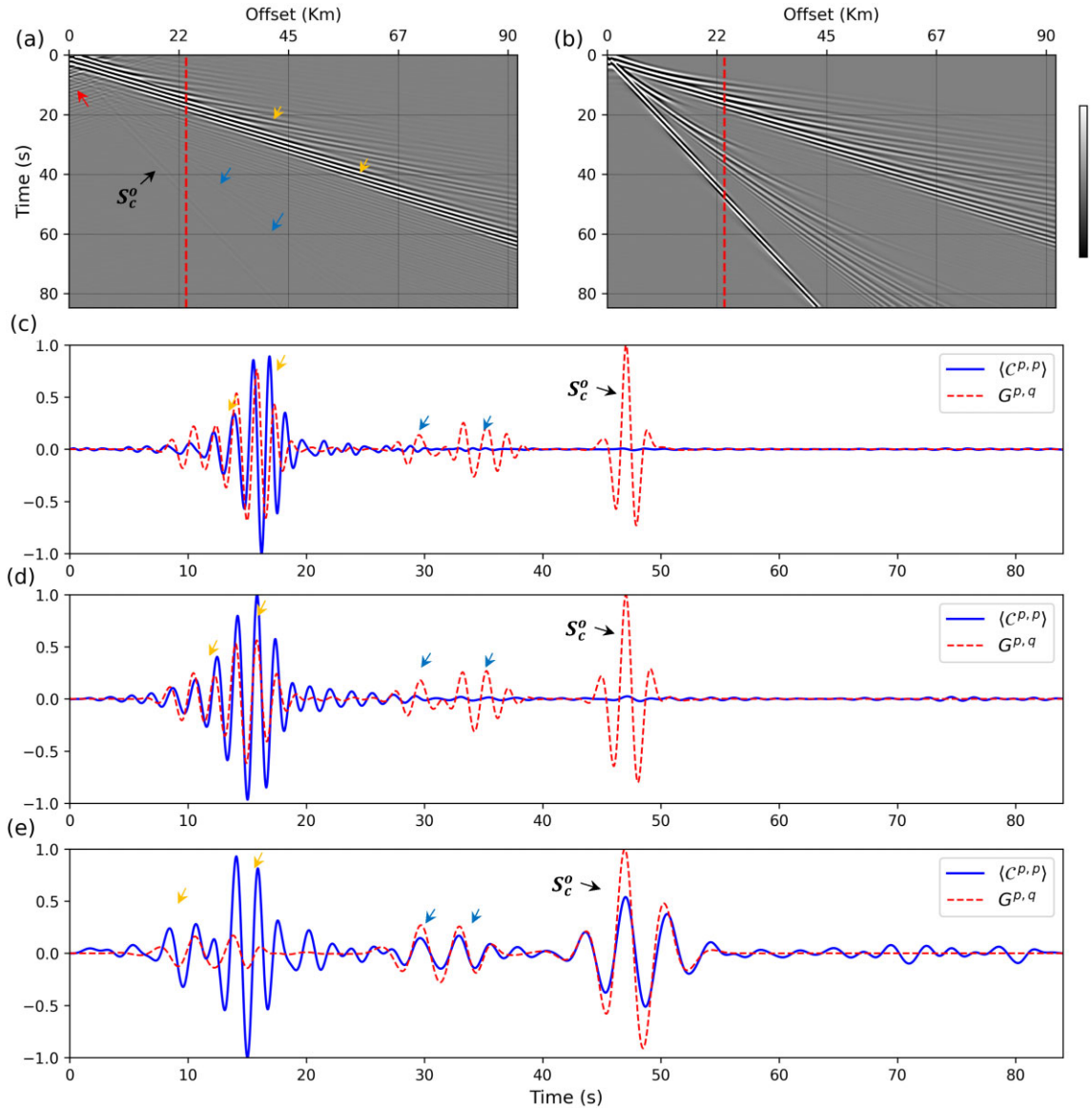


**Figure 12.** Pressure-component: (a) VSG, $\langle \mathcal{C}^{p,p} \rangle$ and (b) Green's function, $G^{p,q}$, for the model shown in Fig. 10. The relative amplitudes between shot gathers are not preserved. (c) Normalized traces from the location indicated by the red line in panels (a) and (b). (d) Traces from (c), low-passed to 0.6 Hz, with $\langle \mathcal{C}^{p,p} \rangle$ uniformly phase-shifted by $-\pi/2$. (e) Traces from panel (d), further low-passed to 0.35 Hz.

near-seafloor shear velocities of approximately 0.5-0.6 km/s (Girard *et al.* 2023). In contrast, the pressure Green's function, $G^{p,q}$, shown in Fig. 12(b), exhibits a clearly visible and strong $S_c^0$ mode along with higher-order modes. The red arrow in Fig. 12(a) indicates spurious cross-mode events.

Fig. 12(c) provides a trace comparison between $\langle \mathcal{C}^{p,p} \rangle$ and $G^{p,q}$ at the location marked by the red lines in Figs 12(a) and (b). Both traces are again normalized to unity. Similar to the observations above, $S_c^0$ and its higher-order mode are barely notable in the full frequency band and the main peaks of the guided P modes also show a misalignment between $\langle \mathcal{C}^{p,p} \rangle$ and $G^{p,q}$. Fig. 12(d) shows the traces after applying a 0.6 Hz low-pass filter, with $\langle \mathcal{C}^{p,p} \rangle$ uniformly phase-shifted by $-\pi/2$. At this stage, the phases of the main peaks of the guided P modes are better aligned; however, Scholte waves are still not visible at these frequencies. To further suppress the guided P modes, we again low-pass filter the traces to 0.35 Hz (Fig. 12e). At this point, $S_c^0$ and its higher-order modes become more visible, and their main peaks align with $G^{p,q}$. However, more spurious events are observed due to cross-mode correlations and imperfect absorbing boundaries.

This example clearly illustrates: (1) the non-convergence of the cross-correlations to Green's functions; and (2) the differential sensitivity of various components CCFs to different wave modes, using a simple velocity model with flat bathymetry and uniform ambient sources on ocean surface. The results highlight the importance of modelling cross-correlations as self-consistent observations, rather than as (exact or approximate) Green's functions, when the conditions required for SI Green's function retrieval are unmet. Significant phase differences are observed between various wave modes in VSGs and the Green's function across different components. If not accurately

accounted for, these differences can introduce significant errors in velocity model building through FWI using cross-correlation gathers. Moreover, other key first-order control factors—such as the ambient energy source mechanism and location, velocity heterogeneity (e.g. the presence of salt bodies), bathymetric variations, and non-uniform ambient source distributions—also can significantly affect wave-mode excitation and partitioning, further emphasizing the complexity of the problem and need for accurate SI wavefield modelling solutions.

## 5 CONCLUSIONS

We derived reciprocity relations for coupled acoustic–elastic media using the constitutive equations governing the coupling at the acoustic–elastic interface, as well as acoustic and elastodynamic reciprocity theorems. From these derivations, we established source–receiver reciprocity expressions for the coupled acoustic–elastic system. Subsequently, we provided an overview of the pressure and velocity Green's function representations in such systems, expressed in terms of wavefield cross-correlations at two observation points within arbitrarily heterogeneous lossless media. Both open and free-surface configurations were considered. For the former, the wavefields are assumed to originate as sources distributed along arbitrarily shaped boundaries enclosing the observation points. For the latter, it is sufficient for sources to exist on an open surface that, together with the free surface, form a boundary enclosing the observation points.

The pressure and velocity Green's function representations are exact but are not directly suitable for SI applications. Specifically, this is because the integrand of these representations comprises a superposition of four correlation products, two arising from the acoustic boundary integral and two from the elastic boundary integral, that must be evaluated separately. The methodology also assumes the availability of specific types of sources at all positions along the enclosing boundary: scalar monopole and dipole sources on the acoustic boundary, and vector force and deformation sources on the elastic boundary. Moreover, these sources are assumed to be impulsive point sources, which often do not align with practical scenarios.

To address these challenges, we adopted a series of approximations to simplify the integrand into two correlation product involving fewer source types. Specifically, monopole sources are used for both states on the acoustic boundary, and monopole *P*- and *S*-wave sources were used for both states on the elastic boundary. We also discussed modifications for scenarios involving uncorrelated ambient sources. In such cases, the representation integral reduces to a direct cross-correlation of the recorded wavefields at two observation points. Finally, recognizing that ideal ambient source distributions rarely exist in practical scenarios, we develop modelling cross-correlation functions as self-consistent observations. This approach, referred to as CCM, only requires assuming uncorrelated ambient sources. It enables more realistic representations of cross-correlations in field data from ambient wavefield studies. We present a synthetic example that simulates a vertical-velocity and pressure component cross-correlation wavefield using CCM, generated by ambient sources distributed across the ocean surface, and compare them with their corresponding Green's functions. Scholte waves are more prominent in the velocity VSGs, while in the pressure VSGs they are barely noticeable across the full frequency band. Additionally, there are significant phase differences between different wave modes identified in VSGs and Green's functions across different components, underscoring the importance of not treating cross-correlated data as Green's functions in the absence of the assumptions required for SI-based Green's function retrieval.

## ACKNOWLEDGMENTS

We gratefully acknowledge the sponsors of the Mines Center for Wave Phenomena Consortium, whose support made this research possible. We also acknowledge the Wendian HPC cluster and Mines Research Computing for providing high-performance computing support for this project. We thank the reviewers, Kees Wapenaar and Yingcai Zheng, for their valuable input during the review process. Lastly, we thank Daniel Peter for his assistance with the SPECFEM3D Cartesian software.

## DATA AVAILABILITY

The synthetic data shown in the numerical examples are available from the corresponding author on reasonable request .

## REFERENCES

Aki, K. & Richards, P.G., 2002. *Quantitative Seismology,* 2nd edn, University Science Books.

Ardhuin, F. & Herbers, T.H., 2013. Noise generation in the solid Earth, oceans and atmosphere, from nonlinear interacting surface gravity waves in finite depth, *J. Fluid Mech.,* **716,** 316–348.

Ardhuin, F., Gualtieri, L. & Stutzmann, E., 2015. How ocean waves rock the Earth: two mechanisms explain microseisms with periods 3 to 300 s, *Geophys. Res. Lett.,* **42**(3), 765–772.

Bakulin, A. & Calvert, R., 2004. Virtual source: new method for imaging and 4D below complex overburden, in *SEG Technical Program Expanded Abstracts 2004,* pp. 2477–2480, Society of Exploration Geophysicists.

Bennethum, L.S., 2006. Compressibility moduli for porous materials incorporating volume fraction, *J. Eng. Mech.,* **132**(11), 1205–1214.

Bojarski, N.N., 1983. Generalized reaction principles and reciprocity theorems for the wave equations, and the relationship between the time-advanced and time-retarded fields, *J. acoust. Soc. Am.,* **74**(1), 281–285.

De Hoop, A., 1966. An elastodynamic reciprocity theorem for linear, viscoelastic media, *Appl. Sci. Res.,* **16,** 39–45.

de Hoop, A.T., 1988. Time-domain reciprocity theorems for acoustic wave fields in fluids with relaxation, *J. acoust. Soc. Am.,* **84**(5), 1877–1882.

de Hoop, A.T., 1990. Reciprocity theorems for acoustic wave fields in fluid/solid configurations, *J. acoust. Soc. Am.,* **87**(5), 1932–1937.
de Ridder, S. & Dellinger, J., 2011. Ambient seismic noise eikonal tomography for near-surface imaging at Valhall, *Leading Edge,* **30**(5), 506–512.
de Ridder, S.A. & Biondi, B.L., 2015. Ambient seismic noise tomography at Ekofisk, *Geophysics,* **80**(6), B167–B176.
Fokkema, J.T. & van den Berg, P.M., 1993. *Seismic Applications of Acoustic Reciprocity,* Elsevier Science Publishing Company, Inc.
Girard, A., Shragge, J., Danilochkine, M., Udengaard, C. & Gerritsen, S., 2024. Observations from the seafloor: ultra-low-frequency ambient ocean-bottom nodal seismology at the amendment field, *Geophys. J. Int.,* **239**(1), 17–36.
Girard, A.J., Shragge, J. & Olofsson, B., 2023. Low-frequency ambient ocean-bottom node surface-wave seismology: A Gulf of Mexico case history, *Geophysics,* **88**(1), B21–B32.
Hasselmann, K., 1963. A statistical analysis of the generation of microseisms, *Rev. Geophys.,* **1**(2), 177–210.
Keinert, B., Innmann, M., Sänger, M. & Stamminger, M., 2015. Spherical fibonacci mapping, *ACM Trans. Graph. (TOG),* **34**(6), 1–7.
Knopoff, L. & Gangi, A.F., 1959. Seismic reciprocity, *Geophysics,* **24**(4), 681–691.
Komatitsch, D. & Tromp, J., 2002a. Spectral-element simulations of global seismic wave propagation—I. Validation, *Geophys. J. Int.,* **149**(2), 390–412.
Komatitsch, D. & Tromp, J., 2002b. Spectral-element simulations of global seismic wave propagation—II. Three-dimensional models, oceans, rotation and self-gravitation, *Geophys. J. Int.,* **150**(1), 303–318.
Komatitsch, D., Barnes, C. & Tromp, J., 2000. Wave propagation near a fluid-solid interface: A spectral-element approach, *Geophysics,* **65**(2), 623–631.
Komatitsch, D. *et al.*, 2023. Specfem/specfem3d: Specfem3d v4.1.0.
Lobkis, O.I. & Weaver, R.L., 2001. On the emergence of the Green's function in the correlations of a diffuse field, *J. acoust. Soc. Am.,* **110**(6), 3011–3017.
Nakata, N., Gualtieri, L. & Fichtner, A., 2019. *Seismic Ambient Noise,* Cambridge University Press.
Pandey, A., Shragge, J. & Girard, A.J., 2025. First-order control factors for ocean-bottom ambient seismology interferometric observations , doi: 10.31223/X5R143.
Rayleigh, J.W.S.B., 1878. *The Theory of Sound,* Vol. **2,** Dover Publications Inc.
Rickett, J. & Claerbout, J., 2000. Calculation of the sun's acoustic impulse response by multi-dimensional spectral factorization, *Sol. Phys.,* **192,** 203–210.
Sager, K., Ermert, L., Boehm, C. & Fichtner, A., 2018. Towards full waveform ambient noise inversion, *Geophys. J. Int.,* **212**(1), 566–590.
Sethi, H., Shragge, J. & Tsvankin, I., 2021. Mimetic finite-difference coupled-domain solver for anisotropic media, *Geophysics,* **86**(1), T45–T59.
Shapiro, N.M., Campillo, M., Stehly, L. & Ritzwoller, M.H., 2005. High-resolution surface-wave tomography from ambient seismic noise, *Science,* **307**(5715), 1615–1618.
Snieder, R., 2004. Extracting the Green's function from the correlation of coda waves: a derivation based on stationary phase, *Phys. Rev. E,* **69**(4), 046 610.
Stewart, P., 2006. Interferometric imaging of ocean bottom noise, in *SEG International Exposition and Annual Meeting,* pp. 1555–1559, Society of Exploration Geophysicists.
Sun, Y.-C., Zhang, W., Xu, J.-K. & Chen, X., 2017. Numerical simulation of 2-D seismic wave propagation in the presence of a topographic fluid–solid interface at the sea bottom by the curvilinear grid finite-difference method, *Geophys. J. Int.,* **210**(3), 1721–1738.
Tromp, J., Luo, Y., Hanasoge, S. & Peter, D., 2010. Noise cross-correlation sensitivity kernels, *Geophys. J. Int.,* **183**(2), 791–819.
van Manen, D.-J., Curtis, A. & Robertsson, J.O., 2006. Interferometric modeling of wave propagation in inhomogeneous elastic media using time reversal and reciprocity, *Geophysics,* **71**(4), SI47–SI60.
Wapenaar, C. & Haimé, G., 1990. Elastic Extrapolation of Primary Seismic P- and S-waves, *Geophys. Prospect.,* **38**(1), 23–60.
Wapenaar, C.P.A. & Berkhout, A.J., 1989. *Elastic Wave Field Extrapolation,* Elsevier.
Wapenaar, K., 2004. Retrieving the elastdynamic Green's function of an arbitrary inhomogeneous medium by cross correlation, *Phys. Rev. Lett.,* **93**(254301), 1–4.
Wapenaar, K. & Fokkema, J., 2006. Green's function representations for seismic interferometry, *Geophysics,* **71**(4), SI33–SI46.
Weaver, R.L. & Lobkis, O.I., 2001. Ultrasonics without a source: thermal fluctuation correlations at MHz frequencies, *Phys. Rev. Lett.,* **87**(13), 134301, doi:10.1103/PhysRevLett.87.134301.
Weaver, R.L. & Lobkis, O.I., 2004. Diffuse fields in open systems and the emergence of the Green's function (L), *J. acoust. Soc. Am.,* **116**(5), 2731–2734.
Zheng, Y., 2010. Retrieving the exact Green's function by wavefield crosscorrelation, *J. acoust. Soc. Am.,* **127**(3), EL93–EL98.
Zheng, Y., He, Y. & Fehler, M.C., 2011. Crosscorrelation kernels in acoustic Green's function retrieval by wavefield correlation for point sources on a plane and a sphere, *Geophys. J. Int.,* **184**(2), 853–859.